SEDIMENTOLOGY the journal of the International Association of Sedimentologists IAS

Sedimentology (2025) **72**, 2323–2360 doi: 10.1111/sed.70043

Sedimentary record of submarine gravity-flow events in the southern Ryukyu forearc during the last 200 000 years: Archive of mega-earthquakes and tsunamis

NATHALIE BABONNEAU* , GUEORGUI RATZOV† , CHARLOTTE GUERIN*, MIRA RICHA*, SERGE LALLEMAND‡ , MICHEL CONDOMINES‡, PATRICK BACHELERY§ , DELPHINE BOSCH‡ , SHU-KUN HSU¶, CHIH-CHIEH SU** , RYUICHI SHINJO††, ANDREW LIN¶ , MARIA-ANGELA BASSETTI‡‡, MARIE REVEL†, ANTONIO CATTANEO* , THE EAGER SCIENTIFIC TEAM[1]

**Geo-Ocean, UMR 6538, Univ Brest, CNRS, Ifremer, Plouzané F-29280, France (E-mail: nathalie.babonneau@univ-brest.fr)*

†Géoazur, Université Côte d'Azur, CNRS, Observatoire de la Côte d'Azur, IRD, 250 rue Albert Einstein, Sophia Antipolis, Valbonne 06560, France

‡Géosciences Montpellier, CNRS, Univ Montpellier, Place Eugène Bataillon, Montpellier 34095, France

§Laboratoire Magmas et Volcans, Université Clermont Auvergne, CNRS, IRD, OPGC, 6 avenue Blaise Pascal, Aubière 63178, France

¶Department of Earth Sciences, National Central University, Chung-Li 32001, Taiwan

***Institute of Oceanography, National Taiwan University, Taipei 10617, Taiwan*

††Department of Physics and Earth Sciences, University of the Ruykyus, 1 Senbaru, Nishihara-cho, Nakagami-gun, Okinawa 903-0213, Japan

‡‡CEFREM, Université de Perpignan Via Domitia, 52 avenue Paul-Alduy, Perpignan 66860, France

Associate Editor: Adam McArthur

ABSTRACT

Despite high convergence velocity, the southern Ryukyu subduction has relatively low and sparse instrumental seismicity, in contrast with the Yaeyama Islands, hit by huge tsunamis over the last few thousand years. This study explores the potential of deep marine sediments to record past large earthquakes and tsunamis. During the MD214/EAGER cruise (2018), four sediment cores (12 to 23 m long) were collected in the forearc area (south of Yaeyama Islands), which is an efficient trap for gravity-flow deposits. The chrono-stratigraphic framework is established with radiocarbon dating, $\delta^{18}O$ stratigraphy, U-series data and tephra analysis including major/trace elements and Hf-Pb-Sr-Nd isotopes. In the basin floor, bulk sedimentation rates locally exceed 60 cm/ka, while hemipelagic sedimentation rates range from 3 to 8 cm/ka, similar to values derived from U-series data in recent sediments of the boxcores. Twenty-four gravity-flow deposits were identified over the last 20 000 years, a frequency consistent with the past tsunamis recorded in the coastal sediments over the last thousand years, emphasising their interest as archives of earthquakes and major tsunamis. At a regional scale, bulk sedimentation rates fall under 10 cm/ka for 48 large-scale gravity-flow deposits over the last 200 000 years. With average recurrence periods about 3500–4000 years, these regional events could be triggered by subduction large earthquakes ($M > 7$). Finally, four exceptionally large submarine gravity-flow events (mega-deposits) of unclear origin have been documented over the last 200 000 years. This work provides an

[1]See Acknowledgements for the List of other participants of EAGER Cruise.

unprecedented time series of major submarine gravity instabilities, probably initiated by great earthquakes on this active subduction. It implies that millennial recurrence periods of great earthquakes must be considered on subduction segments where instrumental seismicity is relatively low and underlines the importance of deep marine sediments in tracing these events.

Keywords Deep-sea gravity flows, earthquake and tsunami records, isotope geochemistry, subduction, tephrochronology, turbidites.

INTRODUCTION

Along subduction zones, the sedimentary record of major submarine gravity-driven processes (submarine landslides, turbidity currents) has been the subject of much work in recent decades to obtain time series of high-magnitude subduction earthquakes and potentially the most devastating tsunamis (e.g. off Cascadia, Goldfinger *et al.*, 2003, 2012; Goldfinger, 2011; in the Caribean area, Feuillet *et al.*, 2011; Beck *et al.*, 2012; Seibert *et al.*, 2024; off New-Zealand, Pouderoux *et al.*, 2014; Pizer *et al.*, 2024; in Indonesian area, Patton *et al.*, 2015; and off Japan, Ikehara *et al.*, 2016, 2018; Usami *et al.*, 2018; McHugh *et al.*, 2020; Kanamatsu *et al.*, 2022). However, linking major submarine gravity-flow deposits with earthquakes is not straightforward, due to the complexity of marine sedimentary systems, their depth and the various factors controlling deep-sea sedimentation (climate, ocean circulation, sea-level, local morphology…) that blur the seismo-tectonic signal (Stow *et al.*, 1985; Covault & Graham, 2010). An accurate analysis of the architecture of the sedimentary bodies, their sediment supply and the possible triggering mechanisms of seafloor instabilities is necessary to select sampling targets (Goldfinger, 2011), also considering the time interval to be explored and the possibilities of obtaining dating or stratigraphic data. Despite the difficulties, in some cases, the sedimentary record of major catastrophic events can be deciphered, providing important and unique information over long timescales of several thousand years for the assessment of natural hazards (Goldfinger *et al.*, 2012; Pouderoux *et al.*, 2014; Patton *et al.*, 2015; Ikehara *et al.*, 2016; Seibert *et al.*, 2024).

Estimating the seismic hazard along the Ryukyu subduction zone has not been extensively carried out, probably because of the lack of instrumental $M > 8$ earthquakes (Kao, 1998). However, the lateral extent of the subduction interface (hundreds of kilometres) and the high rate of convergence >10 cm/yr mean that the possibility of an earthquake of magnitude 8 or even 9 cannot be excluded (Hsu & Sibuet, 2005). Large past tsunamis were reported in the Yaeyama Islands after trenching investigations in the coastal sediments (Ando *et al.*, 2018). The last one is well-known, having occurred in 1771 CE (Goto *et al.*, 2010a).

The Hateruma forearc basin is in the southern part of the Ryukyu subduction zone (Fig. 1). Previous studies have shown that submarine gravity-driven processes dominate the deep-sea sedimentation of the Hateruma area, with sediment coming from the shelf and submarine slope south of the Yaeyama Islands (Kanamatsu *et al.*, 2020; Ikehara *et al.*, 2022). In specific areas where the sedimentation rates are relatively low (lower than 10 cm/ka), it is possible to access thousands of years of records using only a few meters-long sediment cores and the identification of many past submarine gravity-flow deposits through sediment coring is accessible (Xu & Ujiie, 1994; Ujiie *et al.*, 1997; Kanamatsu *et al.*, 2020; Ikehara *et al.*, 2022).

In 2018, new coring data were collected with the R/V Marion Dufresne during the scientific cruise MD214/EAGER (Babonneau & Ratzov, 2018). Four coring sites were investigated with geophysical data (bathymetry and sub-bottom profiler), boxcore sampling and long Calypso piston cores (up to 23.5 m long). Cores have been studied with a wide range of physical, chemical, dating and stratigraphic methods to provide a complete record of submarine gravity-flow processes in the most reliable chrono-stratigraphic framework at time scales from present-day and last centuries to some hundreds of thousands of years.

The main scientific questions are as follows: What are the different gravity-flow processes

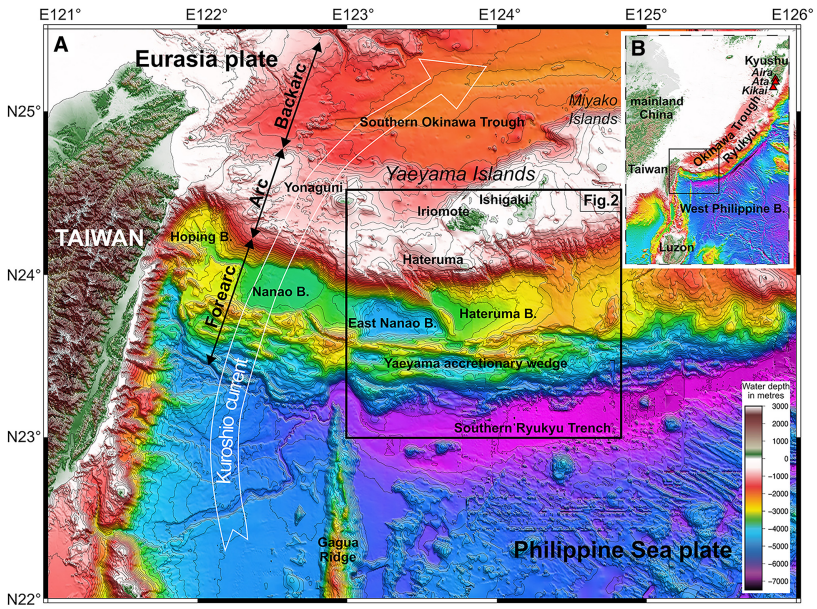

Fig. 1. (A) Bathymetric map focused on the Southern Ryukyu subduction zone, location of the Hateruma forearc basin in the centre of the black rectangle (see in Fig. 2). (B) General location map showing the context of Taiwan at the intersection of the Ryukyu and the Luzon (Manila) subduction zones, in collision with the Chinese continental shelf.

and the sediment sources at the scale of the study area? What are the frequencies and the sizes of the gravity-flow deposits at the different sites? How is it possible to establish a link between these gravity-flow deposits and major earthquakes and tsunamis? In such a context dominated by tectonic and gravity-flow processes, how is the deep-sea sedimentation influenced by sea-level changes or climatic cycles?

REGIONAL SETTINGS

Submarine morphology, geodynamic and regional seismicity

The Ryukyu Island arc is the result of subduction of the Philippine Sea plate beneath the Eurasian plate since the Miocene. The ~E–W trending southern section of the Ryukyu subduction zone propagated westward along a STEP-fault during the last 8 to 10 Ma (Lallemand *et al.*, 2001), thanks to the westward rollback of the South China Sea slab along the Manila Trench. The quasi-transform motion between the Philippine Sea and the Yangtze plates along the southern Ryukyu Trench turned into a north-northwest-dipping subduction in response to the ~N–S opening of the Southern Okinawa Trough (Chen *et al.*, 2021, 2022). Thus, the relative oblique convergence rate between the Philippine Sea plate and the southern Ryukyu forearc varies from ~90 mm/yr near Taiwan up to ~140 mm/yr in the study area (Argus *et al.*, 2011). The accretionary wedge is migrating laterally toward Taiwan because of the high obliquity of the plate convergence causing strain partitioning (Lallemand *et al.*, 1999). The differential motion between the forearc basins and the accretionary wedge is absorbed along a cluster of ~E–W trending transcurrent faults, accounting for a right-lateral motion of 37 ± 7 mm/yr of the accretionary wedge sliver (Dominguez *et al.*, 1998) within a 10 to 15 km wide shear zone running along the outer arc high. The non-volcanic arc is represented by the Yaeyama Islands including two main islands: Iriomote and Ishigaki and several islets like Hateruma located right north of our study area (Fig. 1). Active magmatism is restricted to the southern Okinawa Trough north of the morphological arc. The southern Ryukyu forearc area appears highly segmented.

Several forearc basins are trapped between the southern arc slope and the accretionary wedge, separated by basement highs (Lallemand *et al.*, 1999, 2013). The study area comprises several basins; from west to east, the Hoping and Nanao basin floors are respectively at 3000 m and 3700 m depth, then the 4600 m deep East Nanao basin and the ca 3500 m deep Hateruma basin (Figs 1 and 2). A crescent-shaped ridge culminating at 3000 m of water depth separates the East Nanao basin and the Hateruma basin.

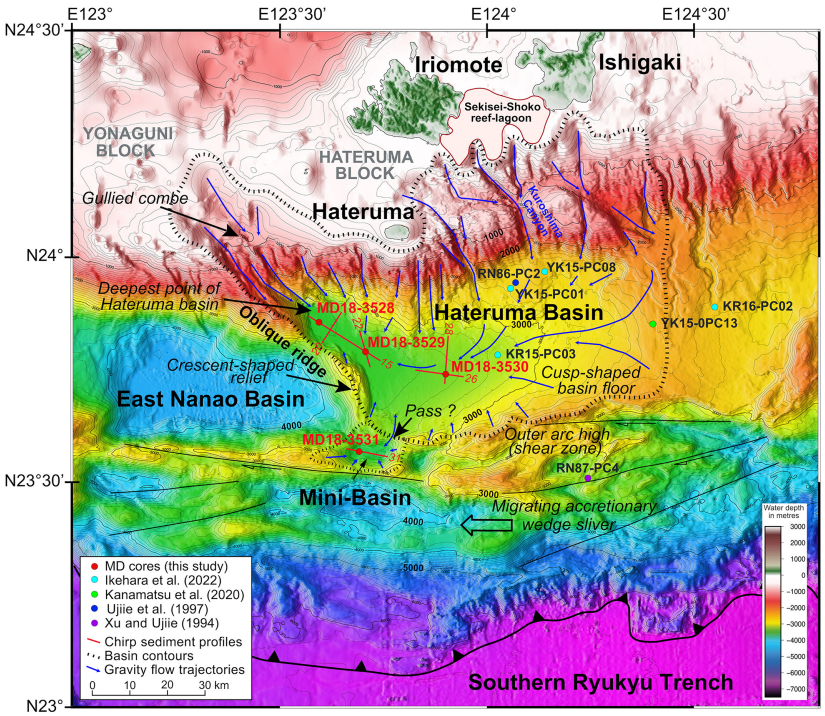

Fig. 2. Bathymetric map focused on the Hateruma forearc basin. The contours of the Hateruma basin and the adjacent mini-basin located at the top of the outer arc high are the tight dotted line. Possible trajectories for gravity-driven flows are indicated with the blue arrows. M214-EAGER sediment cores and Chirp profiles used in this study are in red. A selection of published sediment cores used for the comparison of the EAGER data is also located in this map.

Resulting from the arc–continent collision in Taiwan, the seismicity rate is high near the southernmost termination of the Ryukyu subduction zone. However, despite the fast convergence rate, no great magnitude earthquakes ($M_w > 8$) were reported. The magnitude of the greatest instrumental event, which occurred close to Taiwan in the Hoping Basin region, was re-estimated by Theunissen *et al.* (2010) at M_w 7.7. Further away from Taiwan toward the East, the seismic coupling between the Philippines and Eurasian plates is poorly constrained and probably low but still hotly debated (Arai *et al.*, 2016; Ando *et al.*, 2018; Doo *et al.*, 2018), implying different recurrence times of large magnitude plate interface earthquakes that could exceed 1000 years and could also generate great tsunamis.

Onland records of past tsunamis

The Meiwa tsunami was reported in the Yaeyama Islands in April 1771 CE and caused more than 12 000 casualties (Goto *et al.*, 2010a, 2010b, 2013). This tsunami seems to be a local phenomenon with a run-up from 3.4 to 27.2 m in the Ryukyu Island (Ando *et al.*, 2018) but was not reported along the east coast of Taiwan. This still traumatic event remains puzzling; its source is highly debated among subduction interface earthquakes (Nakamura, 2009), splay fault branched on the plate interface (Hsu *et al.*, 2013), shallow upper plate earthquakes inducing submarine landslides (Miyazawa *et al.*, 2012) or a large gravity collapse of the accretionary wedge (Okamura *et al.*, 2018; Kawamura *et al.*, 2023).

Studies of past tsunamis were based firstly on transported coastal boulders (mostly coral skeleton boulders). They were conducted along the coast of the Yaeyama Islands and the Miyako Islands (Fujiwara *et al.*, 2020b). Many boulders were linked to the 1771 CE event according to radiocarbon dating (Kawana & Nakata, 1994; Suzuki *et al.*, 2008). Some boulders are estimated to be older than 1771 CE and are interpreted as repeated past tsunamis during the thousand years (Kawana & Nakata, 1994; Araoka *et al.*, 2010, 2013; Omoto, 2012). But the difficulties in discriminating between tsunami boulders and storm boulders and in obtaining accurate dating reliable to tsunami age remain high, and this tsunami record remains quite uncertain (Fujiwara *et al.*, 2020b).

The second approach to access to past tsunami records was based on the identification of sandy tsunami deposits in the coastal environments of the Yaeyama and Miyako Islands.

Archaeologists firstly documented the sandy deposits of the Meiwa 1771 CE tsunami (Yamamoto, 2008). Kawana & Nakata (1994) provided the first chronology of past deposits at a millennial scale, coupling studies of coastal sandy deposits and boulders. The most recent work from Ando *et al.* (2018), performed with a 120-m-long trench on the coastal lowland of Ishigaki Island, identified four paleo-tsunami deposits during the last 4000 years. The last deposit was attributed to the Meiwa 1771 CE tsunami and the average recurrence of four large tsunamis is estimated between 600 and 1000 years (Ando *et al.*, 2018). In the same way, the results of Fujita *et al.* (2020) at Mina Island (belonging to Miyako Islands) provide a similar result as Ando *et al.* (2018) and indicate sandy deposits could be reasonably considered as the major tsunami events (excluding the possibility of big storm deposits), with a magnitude equivalent to the Meiwa 1771 event (Fujiwara *et al.*, 2020b).

Climatic, eustatic and oceanographic context during the late quaternary

The climate of the southern Ryukyu area is tropical, mainly influenced by the East Asian Monsoon, which plays a significant role in the local hydrology. It is influenced by the western Pacific subtropical 'Warm Pool', one of the regions with the highest sea surface temperatures and considered a highly typhogenic area (Chen & Huang, 2008).

The regional oceanic circulation is influenced by the Kuroshio Current, which corresponds to the western boundary of the North Pacific Subtropical Gyre, flowing northward along the eastern coast of East Asia. This current transfers heat, salinity and moisture from the Indo-Pacific Warm Pool to the high latitudes (Hu *et al.*, 2015). At present and during interglacial stages, the Kuroshio Current mainly flows through the Yonaguni depression (Fig. 1) toward the Okinawa Trough and the Kuroshio Counter Current, flowing from east to west, is dominant in the forearc basins. However, the trajectory of the Kuroshio Current during the Last Glacial Maximum, with 120 to 130 m less of global sea-level (Lambeck *et al.*, 2014), is still highly debated. The Kuroshio Current could be partly deflected to the east and flow south of the southern Ryukyu Islands (Ujiie & Ujiie, 1999; Ujiie *et al.*, 2003, 2016; Diekmann *et al.*, 2008; Dou *et al.*, 2010, 2012; Fenies *et al.*, 2023). This deflection of the Kuroshio Current pathway during glacial stages could affect East Asia through changes in East Asian Monsoons rainfall patterns (Sasaki *et al.*, 2012), wind propagation (Pan *et al.*, 2018), heat and moisture of the surface ocean, and the ability to generate typhoons (Wu *et al.*, 2008; Liu & Wei, 2015; Fujiwara *et al.*, 2020a; He *et al.*, 2022), and through primary productivity changes (Chen, 2000). However, sea-surface temperature reconstruction (SST) of the Last Glacial Maximum in the East China Sea compiled by Kim *et al.* (2015) indicated no clear difference between inside and outside of the Ryukyu arc, suggesting that the Kuroshio surface water flow was not interrupted into the East China Sea. Moreover, thick deposition of muddy sediments in the southern Okinawa Trough (Diekmann *et al.*, 2008) probably attests a relative continuity of clay feeding from Taiwan, transported by the Kuroshio surface flow to the East China Sea. So, if the Kuroshio Current is deflected to the south of the Ryukyu Islands during the Last Glacial Maximum, it is probably only partially deflected. In any case, sedimentation rates show significant variations between glacial and interglacial periods. Recent work based on a sediment core collected in the Yaeyama accretionary wedge shows a higher sedimentation rate and an increase in primary productivity during the Last Glacial Maximum (Fenies *et al.*, 2023).

Sediment source and distribution in the southern Ryukyu forearc basins

Sediments from the erosion of Taiwan directly feed the Hoping Basin through submarine canyons that merge into the Nanao basin and then, for a small part, into the East Nanao basin (Lehu *et al.*, 2015; Hsiung *et al.*, 2017). The Hateruma basin, 200 km away, more than 1000 m above the East Nanao basin and separated by a crescent-shape relief (Fig. 2), is isolated from the sedimentary input from Taiwan and mainly fed from the Yaeyama Islands to the north via submarine canyons and gullies (Ujiie *et al.*, 1997; Kanamatsu *et al.*, 2020; Ikehara *et al.*, 2022).

At the south of the Hateruma basin, the data published by Xu & Ujiie (1994) concerning the core RN87-PC4 (location in Fig. 2) provided the first long-term record of hemipelagic sedimentation on the accretionary wedge. This core covers the last 110 kyr with a sedimentation rate of about 3 cm/ka and provides a tephrochronologic reference with the Ata tephra around 100 ka BP (Xu & Ujiie, 1994).

Recent studies provide data about clay mineralogy and geochemistry of muddy sediment in the Hateruma basin (Nayak *et al.*, 2021; Garzanti *et al.*, 2023). The composition of clay is clearly dominated by smectite (27–59%), illite + chlorite (36–68%) and kaolinite (4–6%), both in turbidite and hemipelagic layers in the Hateruma basin. The amount of smectite and kaolinite is higher in the Hateruma area than in the western forearc basins, which receive a strong sediment contribution from Taiwan and from the Kuroshio Current (Nayak *et al.*, 2021).

Submarine morphology of the Hateruma basin and the outer-arc high

The Hateruma forearc basin is framed to the north by the unstable slope of the arc, and to the south by the shear zone that coincides with the top of the accretionary wedge, underlined by ridges and small basins offset along a bundle of strike-slip faults. It is limited to the west by a crescent-shaped relief overhanging the Hateruma basin by 500 m and the East-Nanao basin by 1500 m (Figs 1 and 2). Its cusp-shaped floor is gently dipping 0.8° toward the west between 124°25′E (2500 m deep) and 123°45′E (3500 m deep) where it abuts against the crescent-shaped relief. The deepest zone extends north-westward to a depth of 3600 m toward the arc slope, at the base of a gullied combe, oriented NW–SE obliquely to the E–W slope of the arc. As the basin's depocenter is also the deepest point, a sort of narrow sink oriented like the oblique ridge bordering the combe, it is likely to reflect the strong tectonic activity that led to its deepening.

With the improvement of bathymetric data resolution, Kanamatsu *et al.* (2020) described for the first time the detailed submarine morphology south of Ishigaki Island. They identified submarine landslide features. The main sediment source of gravity processes reaching the Hateruma basin comes from the north, that is, from the canyons and gullies incising the slope from the shelf (blue arrows in Fig. 2). A major axis of sediment transfer is from the northwest, where a series of narrow canyons and gullies oblique to the insular slope incised up to the shelf. Another main canyon is located southward from Iriomote and Ishigaki Islands, oriented perpendicularly to the insular slope (Kuroshima Canyon in Fig. 2). Its upper part is composed of several canyon heads incised up to the reef located between Iriomote and Ishigaki Islands (Ikehara *et al.*, 2022). At the base of the steep slope (around cores YK15-PC08 and PC01 in Fig. 2), lobated shape with numerous blocks and irregular morphology, indicating mass-transport deposits, was previously described (Kanamatsu *et al.*, 2020; Ikehara *et al.*, 2022). Given the closed shape of the basin, and even if the submarine reliefs to the east, west and south are lower, contributions from gravity-driven instabilities all around the basin must be considered (as indicated by blue arrows in the Fig. 2).

The innermost region of the accretionary wedge coincides with a shear corridor allowing the wedge to migrate westward under the effect of convergence obliquity. The shear corridor is distributed over several transcurrent faults, isolating small basins bordered by ridges (Fig. 2). These small basins undergo incremental deformation simultaneously with the activation of the boundary faults. Sediment supply from Taiwan is ruled out by the distance and, above all, by the barrier provided by the oblique ridge ending in the crescent-shaped relief that limits the Hateruma basin to the west.

Previous sedimentary records in the Hateruma basin

The sediment core RN86-PC2 (location in Fig. 2) studied by Ujiie *et al.* (1997) was collected at the base of the slope on a fan-like sedimentary body fed by one of the main submarine canyons located to the south of Ishigaki Island. Ten turbidite deposits were identified in the 4 m long core, which covers the last 10 kyr (Ujiie *et al.*, 1997).

Surface-sediment collected in short sediment cores by Kanamatsu *et al.* (2020) is mainly composed of mud, with debrites and rare fine-grained turbidites. Isotopic stratigraphy and correlation of the three cores YK15-01PC03, PC11 and PC13 (location in Fig. 2) reveal a low hemipelagic sedimentation rate and identify the Ata tephra (Kanamatsu *et al.*, 2020).

Recently, Ikehara *et al.* (2022) described in detail a series of canyons located on the northern side of the Hateruma basin and highlighted their connection with coral reefs of Sekisei-Shoko lagoon (Fig. 2). These canyons play an important role in the transport of coarse calcareous material from the reef to the deep-sea, generating coarse calci-turbidites at the toe of the submarine slope (Ikehara *et al.*, 2022). Radiocarbon dating provides recurrence intervals of these turbidites around several hundred

to few thousand years, which could be consistent with recurrences of great tsunamis (Ikehara *et al.*, 2022).

MATERIAL AND METHODS

The data presented in this paper were acquired during the MD214 EAGER oceanographic cruises in June 2018 onboard R/V Marion Dufresne (Babonneau & Ratzov, 2018). It consists of bathymetric data, CHIRP sub-bottom profiles, four Calypso cores (long piston cores) and their associated boxcores at the same location.

Bathymetry and CHIRP profiles

Regional bathymetry used in this study is a compilation including GEBCO 2021 data (doi: 10.5285/c6612cbe-50b3-0cff-e053-6c86abc09f8f), ACT data (Active Collision Taiwan) collected in 1996 onboard the R/V Atalante using a SIMRAD EM12-Dual multibeam system (Lallemand, 1996, https://doi.org/10.17600/96010040). This database provides a MNT with various spatial resolutions with grids from 50 × 50 m to 500 × 500 m and was initially published in Lallemand & Liu (1998).

Published bathymetric data on the eastern part of the Hateruma basin (Kanamatsu *et al.*, 2020), acquired by Japan Oceanographic Data Center under the Hydrographic and Oceanographic Department of the Japan Coast Guard (https://www.jodc.go.jp/vpage/depth500_file_j.html) are added to the bathymetric map. Close to the coring sites and along the chirp profiles, the bathymetry is completed by higher-resolution bathymetric data (20 × 20 m grid) acquired during the MD214 EAGER Cruise with a multibeam echosounder EM112.

Chirp sub-bottom profiler data were acquired along the survey of MD214 EAGER cruise with a SBP120 profiler operating at a frequency that varies between 5300 Hz and 1800 Hz. The penetration of the signal in the sediment is variable up to approximately 80 m and the vertical resolution is about 0.75 m. Unfortunately, the profile connecting the three coring sites in the Hateruma basin was interrupted due to a temporary problem of data acquisition.

Core data and sediment analyses

Coring sites were selected in areas prone to host turbidites through combined analysis of Chirp sub-bottom profiles and bathymetric maps. During the MD214 EAGER cruise, two types of coring systems were used: the giant corer Calypso (up to 30 m long during this cruise) and interface boxcore (1 m long). The water–sediment interface being poorly preserved in Calypso cores, the boxcores thus likely provide complementary data with a good preservation of the seafloor as well as the top 50 to 600 cm of sediment. The reference depth '0' at the top of the boxcore is the true sediment–water interface. If the same deposits are identified in the Calypso core and its companion boxcore, the collected sedimentary succession is complete and continuous in the upper part, with the most recent and present sediment deposits.

Four Calypso cores and companion boxcores were collected in the study area: MD18-3528, MD18-3529, MD18-3530 and MD18-3531. All the characteristics of the cores (location, water depth and length) are shown in Table 1. Three coring sites, MD18-3528, MD18-3529 and MD18-3530, are in the deep part of the Hateruma Basin, at water depths between 3300 m and 3500 m, along a longitudinal WNW–ESE transect (Fig. 2). The fourth coring site, MD18-3531, is in a small basin within the outer-arc high sheared zone, at about 30 km south of the other coring sites. It contains an empty interval of 1.2 m thick, linked to a break in the sediment succession during the coring, caused by the piston suction.

Sedimentary descriptions were carried out with a particular emphasis on sediment colour, visual grain size and sedimentary structures (laminations, bioturbations and contacts), providing the sedimentological logs.

Physical parameters (gamma-density, magnetic susceptibility and P-wave velocity) were acquired with a Multi-Sensor Core-Logger (MSCL; Geotek Ltd, Daventry, UK) on board the R/V Marion Dufresne, with a sampling interval of 1 cm. X-ray radiography (CTscan, Geotek Ltd, Daventry, UK) was later acquired on the core half-sections at Ifremer (Brest, France). Magnetic susceptibility is generally used as an indicator of terrigenous origin, for example, in hemipelagic sedimentation in the China Sea (Liu *et al.*, 2010).

Sediment cores were sampled for grain-size analyses using the Malvern laser grain-size analyzer (Mastersize 2000; Malvern Panalytical, Malvern, UK) at IUEM laboratory (Brest, France), for the 0.01 to 2000 μm fraction. Sample intervals were adapted and chosen according to

Table 1. List of cores, with corer type, location, water depth and length of the sediment cores collected in the study area during the MD214 EAGER Cruise.

Core name	Corer type	Lat N	Long E	Water depth (m)	Core length (m)
MD18-3528	CALYPSO	23°51.19	123°35.77	3502	13.38
MD18-3528 BC	Boxcore	23°51.20	123°35.78	3503	0.15
MD18-3529	CALYPSO	23°46.91	123°42.98	3480	14.79
MD18-3529 BC	Boxcore	23°46.92	123°42.99	3481	0.5
MD18-3530	CALYPSO	23°44.33	123°54.08	3329	22.68
MD18-3530 BC	Boxcore	23°44.34	123°54.09	3330	0.56
MD18-3531	CALYPSO	23°34.14	123°41.52	3591	23.59
MD18-3531 BC	Boxcore	23°34.15	123°41.53	3592	0.61

sedimentary facies. The sampling step-size ranges from 10 to 1 cm in the layers with the most variability. No chemical pre-treatment was carried out before the measurements (no dissolution of carbonates, no deflocculation and no elimination of organic matter). The particle size curve shows the full range of particles, including many foraminifera, but negligible organic matter content.

The chemical compositions of major elements were obtained with the Avaatech XRF core-scanner (Avaatech, BV, Alkmaar, the Netherlands) available at Ifremer (Brest, France). The selected measurement area was 8 mm, and the step-size was set at 1 cm. Each core was analysed at 10 kV and 30 kV. More than 25 major elements were measured. The results are expressed in counts per second (cps), corresponding to a semi-quantitative measurement of the element's content that can be used to assess the vertical variability of the chemical composition in the core. For the interpretation of these curves in marine sediments, calcium Ca is considered a good indicator of carbonate content. Iron Fe indicates the terrigenous fraction. They have opposite trends, allowing the use of the Ca/Fe ratio as a proxy for marine versus terrigenous sediment provenance. The zirconium/rubidium ratio Zr/Rb is often used to evaluate the grain-size variations (Richter *et al.*, 2006; Rothwell & Croudace, 2015; Wu *et al.*, 2020). In the study area, it presents a good consistency with the grain-size measurements. Manganese Mn variations in deep-marine environments indicate redox front and appear useful to identify the end of turbidite decantation and the transition to 'normal' hemipelagic sedimentation in the recent deposits.

Stratigraphy and dating methods

The chronology of sediment cores was obtained by combining several methods: radiocarbon dating on planktonic foraminifera, U and Th-series nuclide measurements (^{210}Pb, ^{230}Th and ^{231}Pa excesses), oxygen isotope stratigraphy and tephra identification.

Radiocarbon dating

Twenty-seven AMS radiocarbon dating results were obtained on the studied cores (Table 2). For each sample, about 10 mg of planktonic foraminifera (*Globigerinae* species) was picked out from the >150 mm fraction, washed in an ultrasonic bath with distilled water and dried. These samples were then analysed at the Beta Analytics Lab (London, UK) and the LMC14 (Paris Saclay, ARTEMIS program). Reported radiocarbon ages were corrected for a marine reservoir effect and converted to calendar years using CALIB Rev 8.2 (Stuiver *et al.*, 1998) with the calibration curve Marine20 (Heaton *et al.*, 2020), and a regional $\Delta R = -40 \pm 31$ (Yoneda *et al.*, 2007). Calibrated kilo years before the present will be referred to as ka cal BP.

U and Th-nuclides in boxcores

Previous works have demonstrated the interest of short-lived nuclides like the $(^{210}\text{Pb})_{ex}$ method to infer the chronology of turbidite deposits of the last century in marine sediments with high sedimentation rates (e.g. Huh *et al.*, 2004, 2006; Dezileau *et al.*, 2016; Lehu *et al.*, 2016).

Table 2. List of samples (10 mg of planktonic foraminifera picked in hemipelagic intervals) sent for AMS radiocarbon dating at two laboratories LMC14 (Paris, Saclay) and Beta-Analytics (London).

Lab. Ref.	Sample	Age BP	Err age BP	2-sigma age cal BP	Median age cal BP
MD18-3528				**DeltaR = −40 ±31 – Marine 21**	
60 309	MD18-3528 44–45 cm	12 370	45	13 588–14 007 cal BP	13 791 cal BP*
59 179	MD18-3528 84–85 cm	8565	35	8868–9266 cal BP	9062 cal BP*
60 310	MD18-3528 415–416 cm	7390	35	7558–7867 cal BP	7709 cal BP
60 311	MD18-3528 440–441 cm	10 785	40	11 828–12 376 cal BP	12 083 ca BP*
Beta – 524 643	MD18-3528 482–483 cm	10 520	30	11 394–11 901 cal BP	11 660 cal BP
Beta – 524 644	MD18-3528 645–646 cm	12 170	40	13 371–13 744 cal BP	13 548 cal BP
Beta – 524 645	MD18-3528 1125–1126 cm	15 190	40	17 345–17 893 cal BP	17 621 cal BP
MD18-3529					
60 312	MD18-3529 126–127 cm	5710	30	5781–6157 cal BP	5962 cal BP
60 313	MD18-3529 145–146 cm	7785	40	7948–8287 cal BP	8106 cal BP
Beta – 524 646	MD18-3529 164–165 cm	9000	30	9408–9742 cal BP	9554 cal BP
59 178	MD18-3529 225–226 cm	10 435	40	11 273–11 763 cal BP	11 523 cal BP
60 314	MD18-3529 260–261 cm	11 595	45	12 768–13 110 cal BP	12 956 cal BP
Beta – 524 647	MD18-3529 309–310 cm	12 180	30	13 396–13 746 cal BP	13 559 cal BP
59 177	MD18-3529 820–821 cm	19 650	90	22 740–23 041 cal BP	22 786 cal BP
MD18-3530					
Beta – 509 556	MD18-3530-BC 17–18 cm	4540	30	4418–4793 cal BP	4600 cal BP
Beta – 509 557	MD18-3530-BC 38–39 cm	7780	30	7951–8274 cal BP	8101 cal BP
Beta – 509 558	MD18-3530 17–18 cm	9520	30	10 114–10 469 cal BP	10 264 cal BP
Beta – 509 559	MD18-3530 125–126 cm	36 000	290	39 568–40 695 cal BP	40 137 cal BP*
59 176	MD18-3530 140–141 cm	40 400	1100	41 745–44 546 cal BP	43 016 cal BP*
MD18-3531					
SacA63725	MD18-3531-BC 34-35 cm	7675	40	7836–8166 cal BP	7995 cal BP
SacA63726	MD18-3531-BC 44–45 cm	8570	40	8867–9275 cal BP	9068 cal BP
Beta – 627 194	MD18-3531-BC 55–56 cm	9020	30	9426–9771 cal BP	9579 cal BP
Beta – 627 195	MD18-3531 24–25 cm	11 270	30	12 498–12 786 cal BP	12 663 cal BP
Beta – 627 196	MD18-3531 44–45 cm	11 480	30	12 705–13 018 cal BP	12 843 cal BP
Beta – 627 197	MD18-3531 63–64 cm	12 340	30	13 571–13 976 cal BP	13 748 cal BP
Beta – 627 198	MD18-3531 122–123 cm	14 670	40	16 733–17 246 cal BP	16 983 cal BP
Beta – 627 199	MD18-3531 129–130 cm	15 060	40	17 188–17 765 cal BP	17 459 cal BP

* Reworked material (inversion).

^{210}Pb, and other useful U and Th-series nuclides, such as ^{230}Th and ^{231}Pa, were then measured by gamma-spectrometry in sediments of the three boxcores MD18-3528-BC, MD18-3529-BC and MD18-3530-BC. The first aim was to check the applicability of the $^{210}Pb_{ex}$ method to get an insight into the sedimentation rates and compare the results with those given by radiocarbon dating. Detailed analytical techniques and data can be found in the Data S1.

Oxygen isotopic stratigraphy

Oxygen isotope analyses were conducted on small batches of *Globigerinoides ruber*, the planktonic foraminifera that calcifies in the surface layer. A total of 221 samples were collected in 1 cm thick sediment intervals, selecting intervals of continuous sedimentation and excluding reworked material (as turbidites): 112 samples for the core MD18-3530 and 109 samples for the core MD18-3531. Cores were subsampled with sample spacing from 2 to 10 cm (adapted to the facies variations). On average, fifteen specimens were picked out from the >150 mm fraction and analysed using a KIEL isotope ratio mass spectrometer (Thermo Fisher Scientific, Waltham, MA, USA) at IUEM (Univ. Brest). The variations in $\delta^{18}O$ obtained along the sediment core are correlated with the LR04 world reference curve issued from benthic foraminifera (Lisiecki & Raymo, 2005) to distinguish the last isotopic stages of the Quaternary and to calibrate its fluctuations over several hundred thousand years.

Tephra analysis

Tephra layers were identified in the sequence based on their high concentration of glass shards, then analysed to track their source and correlate them with other known distal tephra in the area, to finally use them as stratigraphic pointers. To this end, we carried out 258 analyses by EPMA (Electron probe microanalysis) for major element compositions. A selection of eight samples of volcanic glasses (tephra) from one layer in core MD18-3530 and two layers in core MD18-3531 was chosen (258 analyses). Trace element compositions were obtained for a selection of four samples, representative of each tephra horizon, using the LA-ICP-MS (Laser Ablation Inductively Coupled Plasma Mass Spectrometry) method. Sr-Nd-Hf-Pb isotopic compositions were obtained on a selection of volcanic glasses from the same levels using the (MC)-ICP-MS method. The analytical procedures and results are detailed in Data S2.

RESULTS

Surficial structure of the sedimentary succession

The Hateruma basin

Five Chirp profiles are used to describe the superficial structure of the basin infill (Fig. 3). Lines 15 and 26 trending WNW-ESE belong to the same ship track, but the record was interrupted over a few kilometres. Three types of acoustic facies are identified in the Chirp profiles: stratified units, transparent units and chaotic units, giving the metric-scale internal organisation of the depositional units.

Transparent units are thick in the deepest part of the basin and become thinner laterally (Fig. 3). The base of these thick deposits erodes the underlying stratified units. It is particularly visible at the base of the deepest transparent unit (lines 20 and 15 in Fig. 3). The geometry of the transparent depositional units (erosive base and thickening in the deep basin) suggests a gravity-driven origin, and the acoustic facies is similar to 'homogenite' facies, as defined by Cita *et al.* (1996), in the Mediterranean Sea. Four main transparent units (TU1 to TU4) are identified in line 15 (Fig. 3) and are sampled by the long sediment cores MD18-3528 and MD18-3529. The most recent transparent unit located near MD18-3529 shows a complex and irregular shape with two thickening sedimentary bodies (Fig. 3). Chaotic units are characterised by disorganised reflectors, suggesting deformed accumulation as mass-transport deposits. They are several meters thick in lines 15 and 22 (purple in line 15, Fig. 3). The lateral extension of these units in line 26 is unclear. Stratified intervals with low to moderate amplitude in Chirp profiles are typical for marine sedimentation, with parallel reflectors corresponding to pelagic deposits. High-amplitude and continuous reflectors could be related to turbidite deposits (alternating sand/silt and muddy layers).

Mini-basin within the outer-arc high sheared zone

The core MD18-3531 was collected in a small confined basin, named 'mini-basin' at the top of the outer-arc high sheared zone (Fig. 2). The mini-basin floor is 7.5 km long and 3 km wide, at water depth between 3600 m and 3630 m (Figs 2 and 3) with reliefs around between 2700 m and 3500 m of water depth. The sedimentation is fed by hemipelagic sediment and mostly by local gravity-driven processes. It cannot be ruled out that turbidites originating on the insular slope could reach this small basin via a pass located to the northeast of the small basin at a depth of 3200 m (Fig. 2).

The Chirp profile 31 (Fig. 3) crosses the basin floor in the longitudinal axis. It shows a complex geometry of the recent deposits with a structural and morphological high in the centre of the basin. It corresponds to an anticline bounded by two faults reaching the seafloor (Fig. 3). The growth strata support that these structures were recently active. The anticline divides the small basin into two sub-basins, where recent depositions are thicker than at the top of the anticline. The mini-basin infill is characterised by a succession of units with mixed transparent and chaotic units and high-amplitude laminated units (Fig. 3). Depositional geometry also suggests a high contribution of gravity-driven deposits in the basin infill.

Sedimentary facies in the sediment cores

Sedimentary facies are based on lithology, grain size, sorting and sedimentary structures, such as grading, laminations, erosional surfaces and bioturbations (Figs 4 and 5).

Hemipelagic sedimentation

The first sedimentary facies described in all cores is muddy bioturbated accumulations,

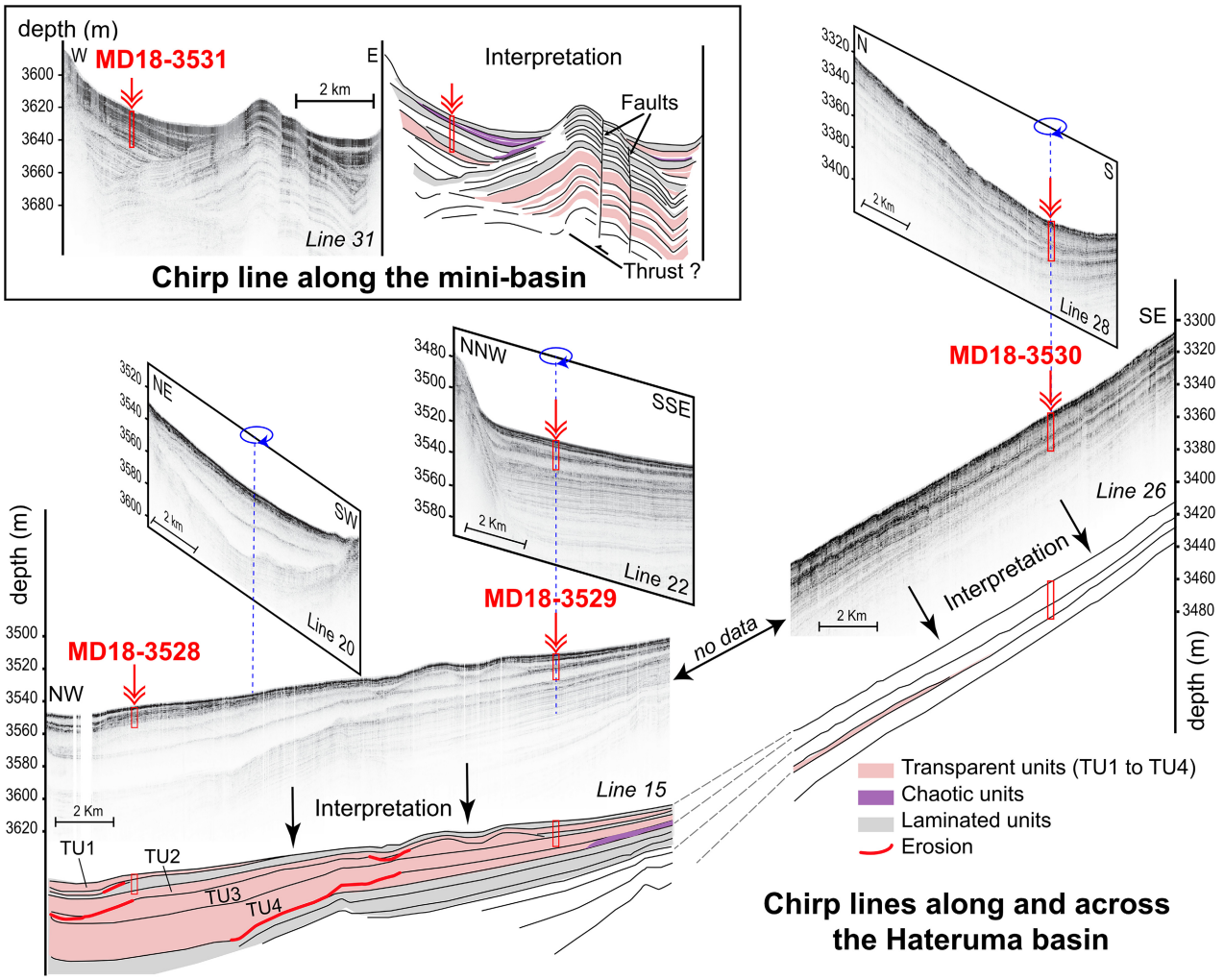

Fig. 3. Chirp profiles (sediment profiler) acquired near the four core sites of the western part of the Hateruma basin and along the mini-basin. The longitudinal profile is a composite profile with line 15 and line 26 (with a data gap of 8 km long between the two profiles) and is presented with a continuous interpretation. The three cross-lines 20, 22 and 28 are displayed in perspective (see location in Fig. 2). Core locations and lengths are indicated in red.

composed of poorly sorted silty-clay. No clear and continuous horizontal laminations are observed. Grain-size measurements provide a median around 10 m to 200 μm (Fig. 4A). Foraminifera are observed in the sieve residue (>63 μm). These facies are interpreted as hemipelagic sedimentation.

Glass shard and pumice-rich layers

Three individual glass shard and pumice-rich layers (hereafter referred to as tephra layer), from 2 to 200 cm thick, are identified in two cores: one in MD18-3530, from 1075 to 1115 cm bsf (below sea floor) and two in MD18-3531, from 600 to 604 cm and from 1495 to 1699 cm bsf. They consist of very-fine sandy layers, with a median grain size around 100 μm (Fig. 4B), mainly composed of small, sharp and vesiculated particles of volcanic glass corresponding to fine volcanic ashes, associated with other components in variable proportions, such as carbonate particles (including numerous microfossils) and mineral grains. The gamma-density of these layers is lower than that of hemipelagic sediment.

The tephra layer of MD18-3530 is a 40 cm thick deposit with sharp basal contact (Fig. 4B and Data S2: Fig. S1). The particle grain size is quite homogeneous with a normal grading along the upper 10 cm. The proportion of glassy

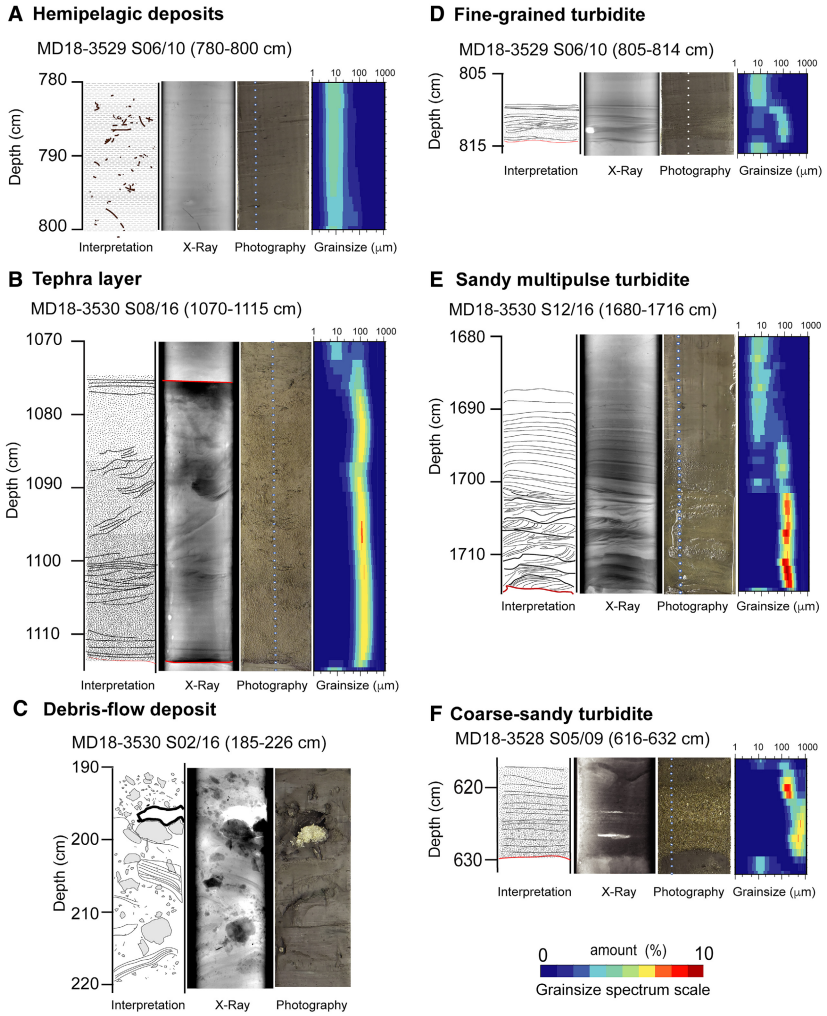

Fig. 4. Sedimentary facies of the main deposit-types identified in the cores: X-Ray radiography, photographs (with the location of the samples for grain-size laser measurements), coloured representation of grain-size distribution.

volcanic fragments varies from around 50% near the base of the deposit to ~80% for a sample in the finer interval between 1087 and 1091 cm bsf (Data S2: Table C).

The upper tephra of MD18-3531 (600 to 604 cm) is ~3.5 cm thick and composed of very-fine particles dominated by volcanic glass (60 to 70%). It is characterised by a sharp basal surface and horizontal laminations of dark and lighter colours.

The lower tephra layer of MD18-3531 (1495 to 1699 cm) is a succession of ~2 m thick multiple layers (amalgamed beds of 5-to-50 cm thick showing normal grading in each individual bed). The grain size ranges from silt to fine sand. The proportion of glassy volcanic particles varies considerably from one bed to another, from less than 10% for some glass-poor laminations to more than 60%. The lithological composition of this thick, bedded tephra layer indicates sediment reworking with various degrees of mixing between glass shards and sediments. All the beds are probably secondary volcanic deposits, but the high content of volcanic particles and their morphology (small, sharp and vesiculated particles) suggest that reworking processes and near-seafloor transport are probably short and occurred shortly after the primary volcanic shard deposition.

Debrites

Some deposits observed in the core MD18-3530 are very disorganised. Their thickness varies from 30 cm to 2.5 m. They are mainly muddy,

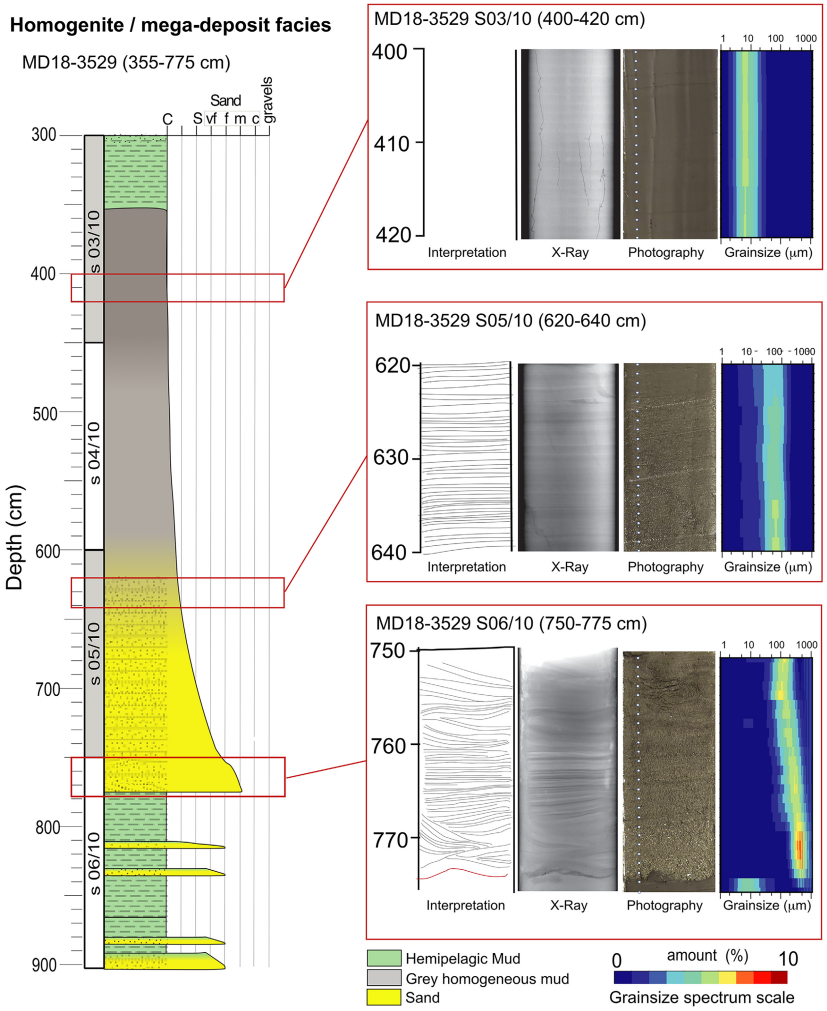

Fig. 5. Sedimentological log showing an example of mega-deposit (mega-turbidite overlaid by an homogenite) identified in the core MD18-3529, details of three sedimentary intervals of this deposit with line-drawing of the sedimentary structures, X-Ray Images, photographs, coloured representation of grain-size distribution.

and most of the biggest elements are mud clasts (centimetric size) with a composition like the matrix. Elements are not sorted, and some are deformed, showing folded internal laminations. The muddy matrix supporting centimetric elements suggests the interpretation of debris-flow deposits or debrite (Mulder & Cochonat, 1996). Note that the most recent debrite of MD18-3530 contains coarse sand, gravel particles and centimetric calcareous fragments coming from coral reefs (block visible in Fig. 4C).

Turbidites

Numerous sandy and silty deposits identified in all cores (Fig. 4D, 4E, 4F) present shared sedimentological characteristics. They all have a sharp or erosional basal contact, horizontal laminations and show normal grading. In some cases, the interval of fine or very-fine sand shows small cross laminations typical of ripple structures. Bioturbations (mainly burrows) are also observed in the upper muddy interval. In the deep marine environment, they typically present the characteristics of turbidites. The grain size at the base of the deposits varies from silt/fine sand (Fig. 4D) to coarse sand (Fig. 4F), and the thickness is also variable from 1 to 2 cm for fine-grained deposits to 3 m for the thickest sandy deposits of MD18-3528.

The silty intervals are generally a few cm thick (<10 cm). They are mainly composed of small particles of quartz. The sandy intervals

generally have a mixed composition. They can be dominated by foraminifera tests and fragments (calcareous source), by quartz and metamorphic particles, as for example micas, amphibole (detrital source) and more rarely by reworked ashes (volcanic source). The thick sandy deposits are dominated by mixed calcareous tests and fragments, such as small fragments of mollusc shells, coral and bryozoan, and benthic and planktonic foraminifera. They are composed of a succession of normally graded layers separated by erosional surfaces. These deposits correspond to multi-pulse sandy turbidites (Fig. 4E) and suggest a simultaneous initiation of multiple turbidity currents, as showed for example by Van Daele *et al.* (2017).

Mega-deposits

Mega-deposits consist of thick deposits (2.5 to 5.5 m thick in the cores), composed of a well-sorted and normally graded sandy layer at the base (median grain size up to 400 μm), fining-upward to a silty interval and covered by a thick homogeneous silty-clay to clay layer (Fig. 5). The sandy and silty intervals are well laminated. Sandy intervals are composed of mixed calcareous and detrital particles and silty terms are clearly dominated by quartz and some metamorphic particles (detrital source). The homogeneous muddy interval is composed of homogeneous grey clay with a low content of silt and without sedimentary structure (no noticeable lamination, no bioturbation, no foraminifera). The average median of grain size is around 8 to 10 μm. The absence of foraminifera indicates that this is the result of a 'gravity' settling of clayey sediment. As foraminifera are coarser and heavier particles than clay, they are concentrated in the basal sandy part of the mega-deposit. This characteristic clearly distinguishes the homogeneous muddy layer of the mega-deposit from a hemipelagic deposit. Such homogeneous muddy layers are documented in other deep-sea contexts as 'homogenite' (Cita *et al.*, 1996; San Pedro *et al.*, 2017). It corresponds to the settling of a large volume of suspended clay, generally associated with a catastrophic event such as a large tsunami, generating the re-suspension of a large sediment volume on the shelves and the upper slopes.

Sedimentary successions in calypso cores

The core MD18-3528 contains 24 sandy turbidites, including a 3 m-thick multipulse sandy turbidite and 2 mega-deposits, interbedded with thin and rare hemipelagic intervals (Fig. 6). In terms of thickness, sandy layers represent 54%, silty layers 6% and muddy layers 40%. Sandy turbidites are enriched in calcium Ca due to the high content of calcareous debris. In contrast, the enrichment in iron Fe follows the clay content and is high in hemipelagic and homogenite layers (XRF curves in Fig. 6). Low values of magnetic susceptibility are visible in calcareous sand, indicating the low content of detrital mineral. Terrigenous sediments are more abundant in the silty fractions, especially in the silty interval of mega-deposits marked by higher values of magnetic susceptibility.

The core MD18-3529 contains a succession of fine-grained and sandy turbidites, and at least two mega-deposits alternating with hemipelagic layers (Fig. 6). In terms of thickness, sandy layers represent 16%, silty layers 8.5% and muddy layers 75.5%. The thick sandy layer at the top of the core could be the base of the most recent mega-deposit.

The core MD18-3530 contains a succession of 67 turbidites (fine-grained and sandy turbidites), 3 debris flow deposits (named DF1 to DF3) and a tephra layer interbedded with hemipelagites (Fig. 7). In terms of thickness, sandy layers represent 12% (including volcanic sand), silty layers 5% and muddy layers 83%. As in MD18-3528 and MD18-3529, sandy and silty turbidites are enriched in Ca and show low Fe content. The tephra deposit, identified at about 11 m bsf (purple in Fig. 7), is characterised by low density and a low Ca/Fe ratio, and grain size ranges from fine to very-fine sand (Fig. 5).

The core MD18-3531 (Fig. 7) is composed of a succession of fine-grained turbidites, sandy

Fig. 6. Sedimentological logs of the Calypso cores MD18-3528 and MD18-3529, curves of gamma density and magnetic susceptibility, curves of the element ratio log(Ca/Fe), coloured representation of the grain-size distribution, median D50, curves of the element ratio log(Zr/Rb), location of radiocarbon dating (red arrows) and median value in ka cal BP, green bands for hemipelagic deposits, yellow for sandy and silty intervals and grey for grey homogeneous mud (homogenite).

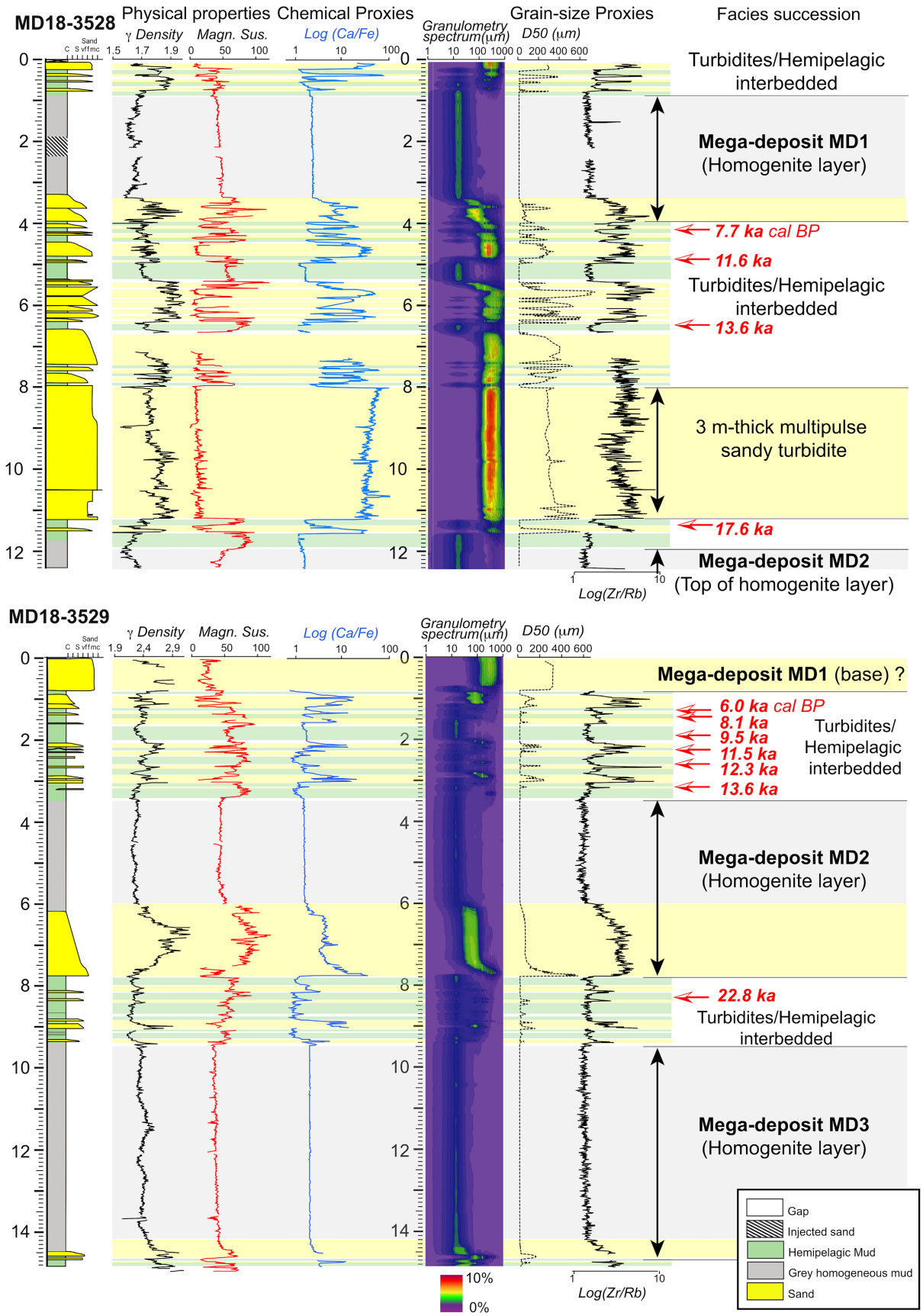

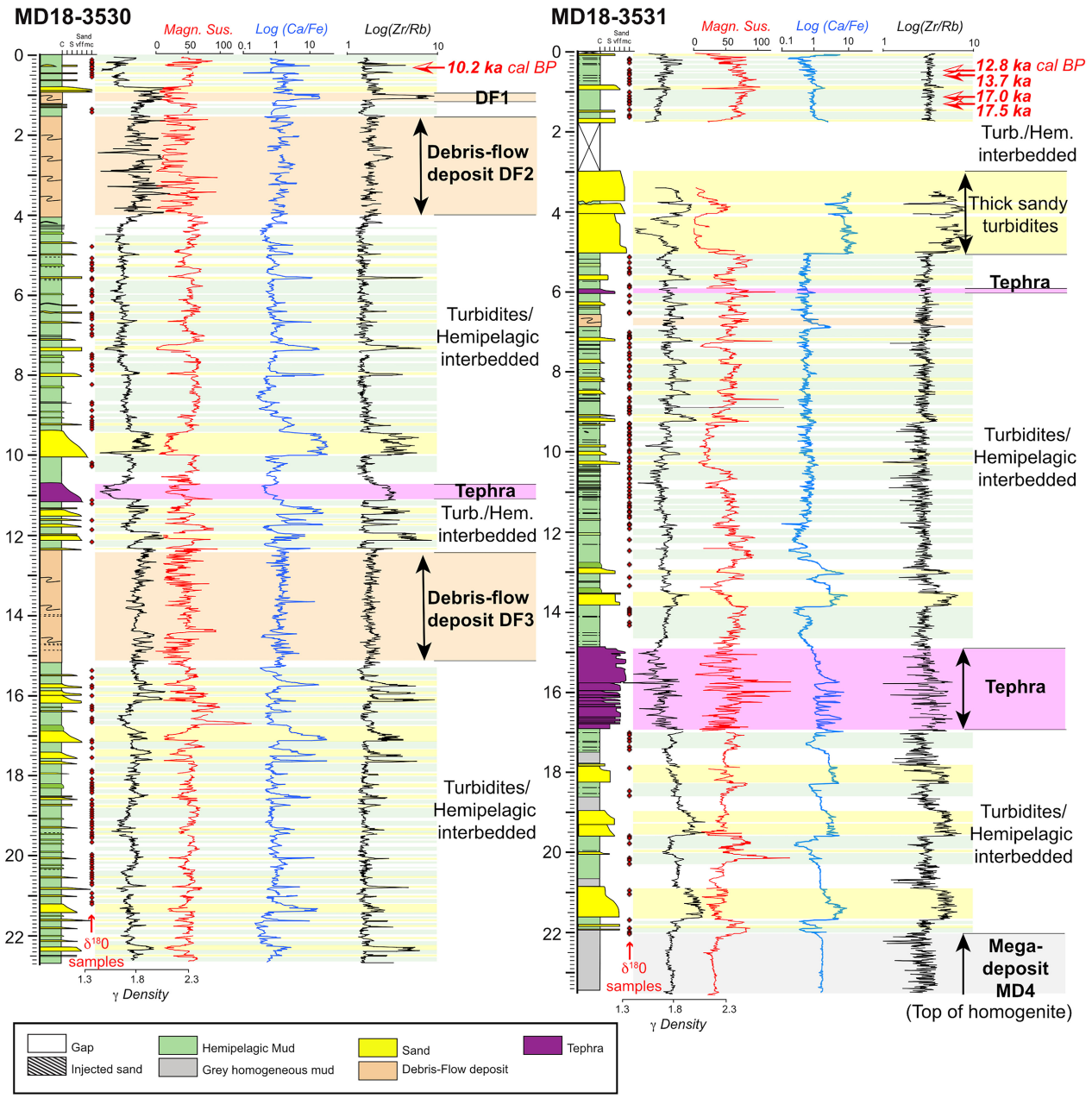

Fig. 7. Sedimentological logs of the Calypso cores MD18-3530 and MD18-3531, curves of gamma density (black) and magnetic susceptibility (red), curves of the element ratio log(Ca/Fe), curves of the element ratio log(Zr/Rb) (black), location of radiocarbon dating (red arrows), samples for oxygen isotopic measurements (red points), median values of radiocarbon in cal BP, green bands for hemipelagic deposits, yellow for sandy and silty intervals, grey for grey homogeneous mud (homogenite), orange for debris-flow deposits and pink for tephra layers.

turbidites and tephra layers interbedded with hemipelagites. In terms of thickness, sandy layers represent 21% (including volcanic sand), silty layers 6.5% and muddy layers 72.5%. A thick sandy deposit is described between 3 and 5 m bsf, composed of a succession of three amalgamated sandy turbidites. The two tephra layers (purple in Fig. 7) are described in the previous section. Below the lower tephra layer, turbidites are thicker than above, with four sandy intervals exceeding 30 cm. The top of these turbidites presents a grey homogeneous clayey

layer. These layers are too thin to be qualified as true homogenite (<40 cm thick) but share similar sedimentological characteristics. Finally, the base of the core MD18-3531 is composed of a 1.5 m-thick homogenite, probably corresponding to the top of a mega-deposit.

Surface sediment in boxcores and continuity with calypso cores

The boxcore MD18-3528-BC is 12 cm long and contains brown hemipelagic silty-clay (Fig. 8). The top of the related Calypso core MD18-3528 begins with a succession of sandy turbidites. There is no common sediment in Calypso and boxcore at this site, indicating a gap of sampling in the last metre of sediment.

The boxcore MD18-3529-BC is 54 cm long and shows two units (Fig. 8). The upper unit between 0 and 29 cm bsf (below the seafloor) is composed of brown mud (silty-clay) and shows laminations in the 23 to 29 cm bsf interval. These laminations correspond to variations in the manganese Mn curve, indicating redox variations in the sediment (Mn high values in Fig. 8). The lower unit between 29 and 45 cm bsf consists of grey homogeneous mud suggesting a homogenite facies. The top of the related Calypso core MD18-3529 consists of a 75 cm-thick sandy layer (Fig. 8). Despite bad preservation of the core top and a possible flowage of sand during the coring process, this sandy layer of the Calypso core could correspond to the basal part of the mega-deposit linked to the homogenite facies described in the boxcore. As for the MD18-3528 site, the connection between Calypso and the boxcore is not possible.

The boxcore MD18-3530-BC is 60 cm long and shows a succession of three fine-grained turbidites interbedded with hemipelagic layers (Fig. 8). Ca/Fe and Zr/Rb ratios highlight three turbidites with the increases in grain size and calcareous debris. The upper part of the deeper turbidite is characterised by grey mud contrasting with the brown hemipelagic mud. The same limit is visible at the top of the Calypso core at 6 cm (Fig. 8). Similar colour contrasts, Ca/Fe and Zr/Rb variations, and radiocarbon dating are consistent to correlate the limit at 51 cm bsf in the boxcore with the limit at 16 cm bsf in the Calypso core (red arrows in Fig. 8).

The boxcore MD18-3531-BC is 60 cm long and shows a muddy succession with subtle colour and grain-size contrasts. Ca/Fe curves indicate two fine-grained turbidites interbedded with hemipelagic layers (Fig. 8). The correlation of the top of the Calypso core and its associated boxcore is also provided by a combined approach including the analysis of the facies succession considering the occurrence of fine-grained turbidites, the variability of chemical ratio (Zr/Rb and Ca/Fe) and the Mn curve (Fig. 8) and the interpretation of radiocarbon dating. Seven radiocarbon ages obtained in hemipelagic sediment allow estimating that the deeper fine-grained turbidite identified in the boxcore could correspond to the uppermost turbidite observed in the Calypso core (Fig. 8).

Core chrono-stratigraphy

Radiocarbon dating and sedimentation rates

Twenty-seven radiocarbon ages were measured (Table 2). Six measurements show reversed ages in the vertical chronology of the cores (in grey in the Table 2). The age inversions indicate that some dating was performed on reworked material. The samples were probably collected at the transition between turbidite, because the top boundary of the turbidite is often difficult to identify accurately.

The calibrated median ages in ka BP are presented in Figs 6, 7 and 8. Uncertainties in the calculation of hemipelagic sedimentation rates are high because of (1) uncertainties of the boundaries determination between hemipelagic and reworked muddy deposits, (2) probable erosion of hemipelagic sediment at the base of gravity-flow deposits and (3) compaction processes inducing differences between surface and buried sediments. The average rates for hemipelagic sedimentation, based on radiocarbon dating, are indicative. They are around 7 to 9 cm/kyr for MD18-3528 and MD18-3529, with cumulative thicknesses of hemipelagic sedimentation of 155 cm above the radiocarbon dating of 17.6 ka cal BP for the core MD18-3528 and 160 cm above the radiocarbon dating of 22.8 ka cal BP for MD18-3529. They are around 3 to 4 cm/kyr for MD18-3530 (31 cm of hemipelagic sediment above the dating of 10.2 ka cal BP) and around 5 cm/kyr for MD18-3531 (100 cm of hemipelagic sediment above the dating of 17.5 ka cal BP). Total sedimentation rates (including gravity-flow deposits) can be calculated using radiocarbon data for the core MD18-3528 and MD18-3529 because of the good vertical distribution of radiocarbon dating along the cores. They are about 64 cm/kyr for MD18-3528 and about 38 cm/kyr for MD18-3529.

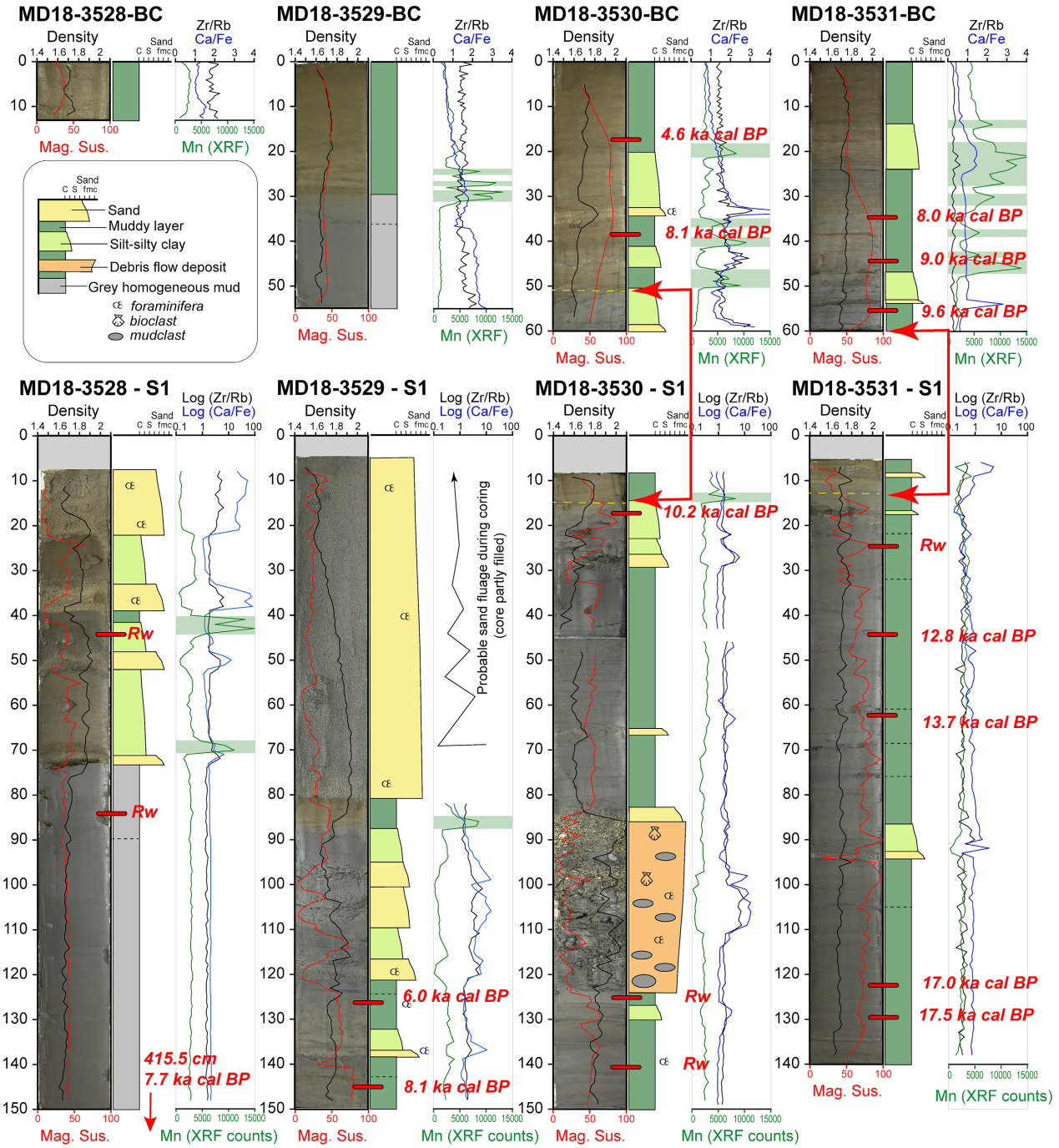

Fig. 8. Sedimentological characterisation of the four Boxcores (top part) and the first sections (S1 – first 150 cm of sediment) of the four associated CALYPSO cores (bottom part) showing photographs, magnetic susceptibility (red curve), gamma density (black curve), sedimentological log (legend below MD18-33528-BC), graphs of major element ratio Log(Ca/Fe) in blue, log(Zr/Rb) in black and variation curve of Mn counts in green, and radiocarbon dates indicated in red (median value ka cal BP, Rw for reworked material).

The base of the core MD18-3528 probably reaches ~18 ka BP and core MD18-3529 could cover the last 25 kyr. The correlation of the two cores with the Chirp profile (line 15 in Fig. 3) provides a good consistency of acoustic transparent units in the Chirp profile with the mega-

deposit in the cores. The lower mega-deposit of MD18-3528 is correlated to the upper mega-deposit of MD18-3529 by the continuity of a transparent acoustic unit (TU2 in the chirp line in Fig. 3). The radiocarbon dating above this mega-deposit, named MD2 in MD18-3528, gives a median age of about 17.6 ka cal BP. Below the MD2 deposit in MD18-3529, the median radiocarbon age is 22.8 ka cal BP. Between the two datings and the MD2 deposit, 20 and 30 cm-thick hemipelagic sediment is preserved, indicating that this event is approximately in the middle of this interval. The MD2 deposit is potentially a good stratigraphic marker dated around 19 to 21 ka BP.

Radiocarbon dates on MD18-3530 and MD18-3531 are limited to the first meters of the core and provide low rates for the total sedimentation. In MD18-3531, the last 20 ka BP are recorded in these first two meters. In MD18-3530, only one radiocarbon dating is available (10 ka BP in the upper part of the first section) indicating a condensation of the sedimentary succession toward the MD18-3530 site.

U and Th-series nuclides in the boxcores of the Hateruma Basin

The upper 10 cm of both MD18-3529-BC and 3530-BC are mainly composed of clay minerals with high Al and K contents in the sediments, and a small proportion of carbonates, estimated at 10 to 13% in the superficial layers (see Data S1: Table B). The proportion of carbonates increases with depth, with higher Ca and lower Al and K contents. The turbidite layers in MD18-3530-BC have the highest carbonate content (e.g. around 25% for the 41 to 42 cm layer), and the muddy layers composing the upper part of turbidites are also carbonate-rich. Because of the often-difficult distinction between muddy turbidites and typical hemipelagic sediments, we consider that these latter are best represented by the upper 10 cm of sediment with high Al and K contents.

$^{210}Pb_{ex}$ data. The Fig. 9A and 9B display ^{210}Pb, ^{226}Ra and $^{210}Pb_{ex}$ versus depth for MD18-3530-BC and 3529-BC. In the first 8 to 10 cm, ^{226}Ra tends to slightly increase with depth in both cores, and the $^{210}Pb_{ex}$ profiles are similar and show a rapid decrease with depth. The ^{226}Ra profiles can be explained by its loss by diffusion from the sediment to bottom seawater, as observed and modelled in sediments from NE Pacific by Kemnitz *et al.* (2023). Although displaying some outliers, the $^{210}Pb_{ex}$ profiles of the first 10 cm can be reasonably fitted by an exponential curve. Interpreted in terms of sedimentation (v) or mass accumulation (w) rates, these data would give sedimentation rates of 64 cm/kyr and 110 cm/kyr (or 54 g/cm^2/kyr and 92 g/cm^2/kyr) for MD18-3530-BC and 3529-BC respectively.

These values are around a factor of 16 higher than the sedimentation rates derived from ^{14}C ages (see Section 4.5). Exponential decreases of $^{210}Pb_{ex}$ are frequently observed in superficial sediments of deep oceanic basins (e.g. Henderson & Anderson, 2003) and they are usually explained by an advection–diffusion process due to bioturbation in the upper mixed layer of the sediment. It is thus most likely that the observed $^{210}Pb_{ex}$ profiles in the boxcores result from the same process, which has been modelled by Guinasso & Schink (1975) and Anderson *et al.* (1988). They showed that the evolution of the activity A of the nuclide with depth z can be described by an exponential equation:

$$A = A_0.\exp\left[\frac{v-\sqrt{(v^2+4\lambda D)}}{2D}z\right] \quad (1)$$

where D (or D_B) is the mixing coefficient in cm^2/yr. Assuming that the true sedimentation rates v are those derived from the younger ^{14}C ages measured in the MD18-3529 and MD18-3530 cores, mixing coefficients of 0.25 cm^2/yr and 0.12 cm^2/yr can be calculated for cores MD18-3529-BC and 3530-BC respectively. They fall in the range found in most deep oceanic sediments (Boudreau, 1994; Henderson & Anderson, 2003), and are comparable to mixing coefficients calculated by Yang *et al.* (1986) from $^{210}Pb_{ex}$ profiles in NW Pacific deep sediments (0.1 to 0.6 cm^2/yr).

Another argument to discard $^{210}Pb_{ex}$ data as indicative of sedimentation rates is provided by the data of artificial, bomb-related ^{137}Cs and ^{241}Am radionuclides that reached their peak activities in the atmosphere around 1963. They are only present in the upper 4 cm of both MD18-3529-BC and 3530-BC. Moreover, in the MD18-3530-BC, with the lower mixing rate, most of the activity is found in the surface layer. If the highest ^{137}Cs and ^{241}Am activities found in the upper 0.5 cm of the MD18-3530-BC correspond to the 1963 atmospheric peak, then the sedimentation rate should be lower than 0.009

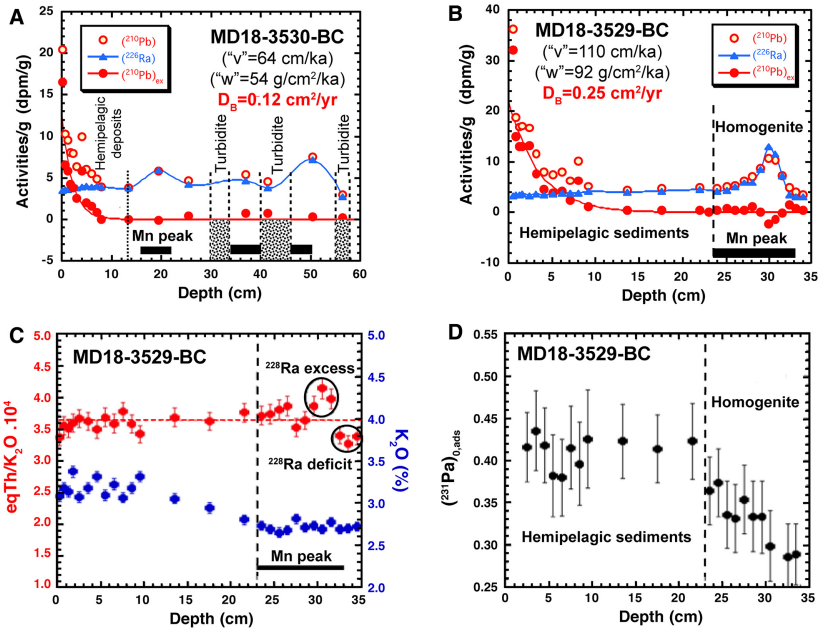

Fig. 9. (A) Activities/g of ^{210}Pb, ^{226}Ra and $(^{210}Pb)_{ex}$ versus depth z in MD18-3530-$_{BC}$. While (^{226}Ra) slightly increases in the upper 10 cm of hemi-pelagic sediments (HS), it shows significant variation in the deeper sediment layers. The ^{226}Ra peaks are correlated with the Mn peaks, which develop near the top of layers overlying a turbidite (T). The (^{210}Pb) evolution parallels the evolution of (^{226}Ra). The $(^{210}Pb)_{ex}$ profile is the result of sediment mixing, with a calculated mixing coefficient D_B of 0.12 cm^2/yr. Interpreted in terms of sedimentation rates ('*v*' or '*w*'), this profile would give unrealistic rates. (B) Activities/g of ^{210}Pb, ^{226}Ra and $(^{210}Pb)_{ex}$ versus depth z in MD18-3529-$_{BC}$. The apparent ^{210}Pb deficit centred on the ^{226}Ra peak is due to a recent ^{226}Ra adsorption onto MnO_2. The $(^{210}Pb)_{ex}$ profile allows calculation of a mixing coefficient D_B of 0.25 cm^2/yr. (C): K_2O and eqTh/K_2O ratios versus depth in the MD18-3529-$_{BC}$ core. eqTh means equivalent Th, assuming ^{232}Th-^{228}Ra equilibrium. The smaller K_2O content in the lower part of the core results from a dilution due to the higher carbonate content of these layers overlying a turbidite. However, as Th and K are both essentially contained in clay minerals, their ratio remains nearly constant, except near the Mn peak, due to ^{228}Ra excesses or deficits. (D) $(^{231}Pa)_{0,ads}$ (in dpm/g) versus depth in the MD18-3529-$_{BC}$ core. $(^{231}Pa)_{0,ads}$ is nearly constant in the upper hemipelagic sediments but has lower values below 23 cm depth, in layers with higher carbonate contents (homogenite) overlying a turbidite (see text for further discussion).

cm/yr or 9 cm/kyr [0.5/(2020–1963)], in agreement with sedimentation rates derived from ^{14}C dates.

^{226}Ra mobility and its influence on $^{210}Pb_{ex}$ profiles. Below the upper 10 cm, ^{226}Ra displays significant variations in MD18-3530-$_{BC}$ (Fig. 9A). But the largest ^{226}Ra values are found in the core MD18-3529-$_{BC}$, at around 30 cm depth (Fig. 9B). The ^{226}Ra peaks in both MD18-3530-$_{BC}$ and MD18-3529-$_{BC}$ occur at the same depth as the Mn peaks (Fig. 8), whose position is also reported in Fig. 9. The Mn peaks are interpreted as the result of MnO_2 precipitation at the sediment–water interface after an episode of turbidite and homogenite deposition (Polonia *et al.*, 2012; McHugh *et al.*, 2016). ^{226}Ra is easily absorbed onto MnO_2, and the correlation between the ^{226}Ra and Mn peaks is thus not surprising. The nearly superimposed ^{226}Ra and ^{210}Pb profiles suggest that most ^{210}Pb is radiogenic ^{210}Pb produced by ingrowth from adsorbed ^{226}Ra that reached radioactive equilibrium with ^{226}Ra. This example demonstrates the importance of measuring both ^{210}Pb and ^{226}Ra for each analysed layer, instead of extrapolating ^{226}Ra values measured in the upper layers or taking the supported ^{210}Pb value at depth as a measure of ^{226}Ra. Such estimations would have resulted in artificial $^{210}Pb_{ex}$ peaks.

Besides this enrichment in ^{226}Ra linked to MnO_2 precipitation following the turbidite deposition, there is also evidence of recent mobility of Ra isotopes. A detailed examination of

the $^{210}Pb_{ex}$ profile around the Mn and ^{226}Ra peaks of MD18-3529-BC suggests that ^{226}Ra adsorption onto MnO_2 might also have occurred recently, that is, in the last decades. Indeed, ^{210}Pb deficits are present at the same depth as the ^{226}Ra peak and small ^{210}Pb excesses are found just below this peak (Fig. 9B). Such disturbances probably result from recent adsorption onto MnO_2 of ^{226}Ra transported by the upward movement of fluids, due to sediment compaction and/or bioturbation and/or to expulsion of fluids resulting from earthquake-induced shaking.

Moreover, this recent mobility also affects ^{228}Ra, the other relatively long-lived Ra isotope ($T = 5.75$ yr). This is illustrated in Fig. 9C, where apparent ^{232}Th excesses and deficits are present in and below the layer showing the Mn peak (Fig. 9C and Data S1). This ^{228}Ra redistribution must necessarily have occurred within the last 30 yr.

Long-lived nuclides ^{230}Th and ^{231}Pa. Although ^{230}Th and ^{231}Pa are difficult to analyse by gamma-spectrometry and can only be measured with large uncertainties (see analytical techniques in Data S1), their interest in studies of oceanic sedimentation justifies consideration of these results. Indeed, ^{230}Th, produced by the decay of ^{234}U in the ocean, is quantitatively adsorbed onto particles and transferred to the sediment. In the absence of lateral import or export of sediments, the activity/g of adsorbed ^{230}Th measured in sediment, $(^{230}Th)_{ads}$, can be directly related to the mass accumulation rate of sediment w (g/cm^2/yr) at a given water depth (e.g. Francois *et al.*, 2004). Indeed, the ^{230}Th flux F_{Th} (e.g. in dpm/cm^2/yr) produced in a water column of depth z (m) with a given (^{238}U) activity (dpm/L) and the ($^{234}U/^{238}U$) activity ratio of seawater ($R = 1.147$) is simply:

$$F_{Th} = 0.1\lambda_{230}\, R\left(^{238}U\right) z \qquad (2)$$

$$\left(^{230}Th\right)_{ads}\,(\mathrm{dpm/g}) = F_{Th}/w \text{ or } F_{Th}/\rho v, \qquad (3)$$

$(^{230}Th)_{ads}$ is calculated by subtracting from the measured ^{230}Th the supported ^{230}Th (in radioactive equilibrium with ^{238}U in the detrital component) and the radiogenic ^{230}Th produced by ^{234}U decay in the authigenic minerals like carbonates or Fe, Mn oxides (e.g. eq. [18] in Francois *et al.*, 2004).

^{231}Pa is less particle-reactive than ^{230}Th but is still useful in discussing sedimentation processes. In particular, the $(^{231}Pa)_{ads}/(^{230}Th)_{ads}$ ratio is often used as an indicator of particle fluxes in the ocean, or biological productivity in oceanic areas where most particles are of biogenic origin, like in the South Pacific (e.g. Henderson & Anderson, 2003; Chase, 2008). $(^{231}Pa)_{ads}$ is calculated in a similar way as $(^{230}Th)_{ads}$, by subtracting from the measured (^{231}Pa) activity the supported activity (in equilibrium with ^{235}U in the detrital component) and the radiogenic ^{231}Pa produced by decay of ^{235}U in authigenic minerals.

Corrections for both radiogenic ^{230}Th and ^{231}Pa are negligible, since most U is of detrital origin, as confirmed by the crustal Th/U ratios close to 5 (Table 3). The initial $(^{230}Th)_{0,ads}$ and $(^{231}Pa)_{0,ads}$ values at the time of deposition of each sediment layer are calculated using the ages t interpolated from the ^{14}C dates, following the usual equation: $A_0 = A.\exp(\lambda t)$.

Weighted average values of $(^{230}Th)_{0,ads}$ and $(^{231}Pa)_{0,ads}$, and the $(^{231}Pa)_{0,ads}/(^{230}Th)_{0,ads}$ ratio are calculated from the data of the upper 10 cm of cores MD18-3529-BC and 3530-BC, which are thought to best represent typical hemipelagic sediments (Table 3). The average values of $(^{230}Th)_{0,ads}$ are then used to calculate the sedimentation rates from Eq. (3). The ^{230}Th flux F_{Th} is estimated from Eq. (2), using the average U content measured by Chen *et al.* (1986) in Pacific waters at 31° N (3.26 ng/g). The calculated mass (w) and linear (v) accumulation rates are reported in Table 3. *w* varies from 2 to 2.8 g/cm^2/kyr and *v* from 2.4 to 3.9 cm/kyr. These sedimentation rates are smaller than those calculated from the most recent ^{14}C dates for MD18-3529-BC (3.6 cm/kyr compared to 6.8 cm/kyr) and 3530-BC (2.4 cm/kyr compared to 3.7 cm/kyr) but are clearly of the same order of magnitude. The difference between the calculated rates might be explained by a lateral import of sediment, with 'focusing factors' f (Francois *et al.*, 2004) of 1.9 and 1.5 for MD18-3529-BC and 3530-BC respectively. In any case, the rates derived from adsorbed ^{230}Th confirm the low hemipelagic sedimentation rates in the Hateruma Basin.

Average $(^{231}Pa)_{0,ads}/(^{230}Th)_{0,ads}$ ratios in the top hemipelagic sediments vary from 0.09 ± 0.02 (MD18-3528-BC and 3530-BC) to 0.13 ± 0.02 in BC 3529. The first value is similar to the production ratio of these radionuclides in oceanic seawater (0.093). The higher ratio in MD18-3529-BC could reflect lateral transport of the less particle-reactive ^{231}Pa (compared to ^{230}Th) by advection or diffusion toward a zone of high particle flux

Table 3. Average values of K_2O, Th, U, $(^{230}Th)_{0,ads}$ and $(^{231}Pa)_{0,ads}$ in MD18-3528-BC, 3529-BC and 3530-BC boxcores, for the upper layers considered as typical hemi-pelagic sediments. The reported uncertainties are 1σ standard deviations of the data (the number of analyses is $n = 3$, 12 and 11 for MD18-3528-BC, 3529-BC and 3530-BC respectively). w and v are the mass and linear accumulation rates derived from the initial adsorbed ^{230}Th, $(^{230}Th)_{0,ads}$.

Cores (water depth)	K_2O (%)	Th (ppm)	U (ppm)	Th/U	$(^{230}Th)_{0,ads}$ dpm/g	$(^{231}Pa)_{0,ads}$ dpm/g	$(^{231}Pa/^{230}Th)_{0,ads}$	W (g/cm^2/ka)	V (cm/ka)
MD18-3528-BC (3511 m)	2.53 ± 0.13	9.21 ± 0.44	1.91 ± 0.16	4.81 ± 0.55	3.45 ± 0.8	0.304 ± 0.029	0.088 ± 0.022	2.7 ± 0.2	3.9 ± 0.7
MD18-3529-BC (3480 m)	3.18 ± 0.10	11.4 ± 0.3	2.42 ± 0.18	4.72 ± 0.36	3.19 ± 0.73	0.126 ± 0.017	0.126 ± 0.017	2.8 ± 0.4	3.6 ± 0.7
MD18-3530-BC (3329 m)	3.07 ± 0.03	11.3 ± 0.2	2.25 ± 0.19	4.99 ± 0.45	4.39 ± 0.88	0.091 ± 0.018	0.091 ± 0.018	2.0 ± 0.4	2.4 ± 0.6

at the MD18-3529 site (Henderson & Anderson, 2003, 2003b). This is coherent with the higher sedimentation rate observed at this site (Table 1). Such correlations between the $(^{231}Pa)_{0,ads}/(^{230}Th)_{0,ads}$ ratios and the sedimentation rates are indeed commonly observed (Henderson & Anderson, 2003 and references therein).

It should be noted that both $(^{230}Th)_{0,ads}$ and $(^{231}Pa)_{0,ads}$ have lower activities/g in the lower layers of MD18-3529-BC and 3530-BC (see Data S1). This is illustrated for $(^{231}Pa)_{0,ads}$, where $(^{231}Pa)_{0,ads}$ is plotted versus depth in MD18-3529-BC (Fig. 9D). As the proportion of carbonates is higher in these layers, the lower $(^{231}Pa)_{0,ads}$ values partly result from a dilution of the clay component, ^{231}Pa being certainly less adsorbed onto carbonate particles than onto clay minerals (Chase *et al.*, 2003). But the lowest $(^{231}Pa)_{0,ads}$ values suggest an origin of this sediment, interpreted as homogenite overlying a turbidite layer, from areas at shallower depth, with smaller $(^{231}Pa)_{0,ads}$ values.

$\delta^{18}O$ isotopic stratigraphy

$\delta^{18}O$ curves obtained along the cores MD18-3530 and 3531 are interpreted in comparison to the global reference curve for benthic foraminifera LR04 (after Lisiecki & Raymo, 2005), providing the limit of the Marine Isotopic Stages (MIS) and also in comparison with regional curves obtained on planktonic foraminifera. In Fig. 10, the $\delta^{18}O$ curves in the core RN87-PC4 (Xu & Ujiie, 1994), located to the south of the Hateruma basin (Fig. 2) and in the core MD01-2422 (Matsu'ura *et al.*, 2021), located to the east of Kyushu Island (Fig. 2), are also displayed.

Along the cores MD18-3530 and 3531, values of $\delta^{18}O$ vary between −0.3‰ and −2.3‰ (Fig. 10 and Data S3). The heavy values in planktonic foraminifera are interpreted as corresponding to glacial stages and the low values as interglacial stages. The top of both cores is calibrated with the radiocarbon ages and shows good consistency of isotopic data for the last 20 ka BP (Fig. 10). To facilitate the interpretation, $\delta^{18}O$ curves are displayed along a vertical column corresponding to the cumulated thickness of hemipelagic deposits alone, with subtraction of instantaneous gravity-flow deposits. The corrected depth determination without turbidites is provided in the Data S4. Despite a gap of $\delta^{18}O$ data during the MIS 2 in core MD18-3530, the succession of MIS 3 to MIS 7 is identified, providing the stratigraphy of MD18-3530 over the last 200 kyr (Fig. 10). Similarly, the

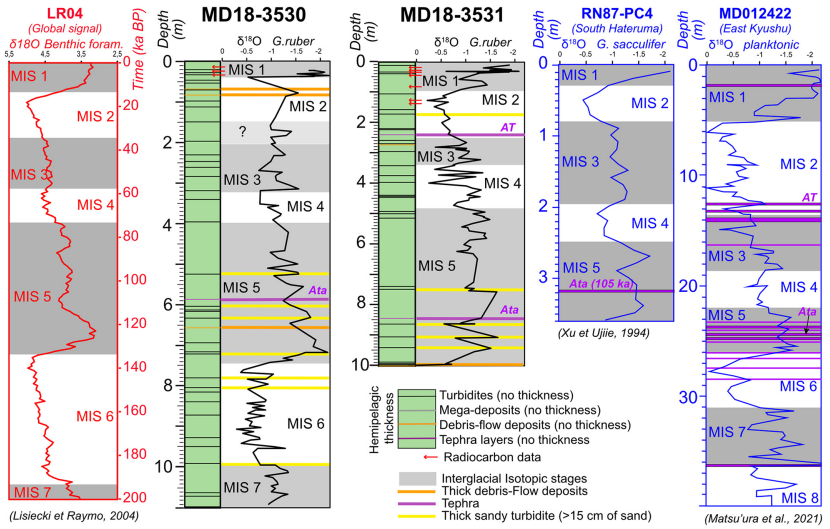

Fig. 10. Global curve of $\delta^{18}O$ of benthic foraminifera established by Lisiecki & Raymo (2005) for the last 200 kyr (in red), cumulated hemipelagic successions for the cores MD18-3530 and MD18-3531 with $\delta^{18}O$ curves measured on planktonic foraminifera (G. ruber), regional curves of $\delta^{18}O$ measured on planktonic foraminifera for core RN87-PC4 (from Xu & Ujiie, 1994) and for core MD01-2422 (from Matsu'ura *et al.*, 2021).

interpretation of the $\delta^{18}O$ data of MD18-3531 provides the stratigraphic boundaries from MIS 1 to MIS 5 (Fig. 10). In MD18-3531, the MIS 5 is particularly thick, with an estimation of 5.5 m of cumulated hemipelagic sedimentation. This abnormal thickness could be the result of the difficulty in determining the muddy interval of turbidite and the true hemipelagic layers (sedimentological, physical and chemical characteristics are similar in this core). The tephra layers identified in the middle of the MIS 5 (purple line in Fig. 10) could be used as a stratigraphic marker and may correspond to the Ata eruption identified in the core RN87-PC4 (Xu & Ujiie, 1994).

The $\delta^{18}O$ stratigraphy provides average hemipelagic sedimentation rates of around 5 cm/kyr for MD18-3530 and around 7.6 cm/kyr for MD18-3531, slightly higher than the value calculated with radiocarbon data but of the same order. For the total sedimentation rate, including gravity deposits, the values are, respectively, about 10.6 cm/kyr for MD18-3530 and 20 cm/kyr for MD18-3531.

Tephra analysis

Eight samples were selected (Data S2, Table C) to characterise the texture and chemical composition of the three tephra layers identified in the cores MD18-3530 and MD18-3531. In all samples, the volcanic particles are thin, colourless and transparent glassy fragments, typical of bubble-wall glass shards and pumice fragments with mostly elongated vesicles (Fig. 11 and Data S2: Fig. S1). The shards have fluidal shapes, with spiny, flat, cuspate or fibrous morphologies, up to 300 μm in the longest axis. There are no signs of alteration. This pyroclastic material is associated, in variable proportions, with carbonate particles (including foraminifera) and magmatic crystals (quartz, feldspar, apatite, titanite, ortho- and clino-pyroxenes, amphibole, biotite, Ti-magnetite). Among these different mineral phases, some (quartz, feldspar, orthopyroxene) can be seen surrounded by a thin coating of volcanic glass with the same composition as the other glass shards, indicating their link (Data S2: Fig. S1).

The composition of the glass shards analysed within the same tephra layer is homogeneous, with a unimodal distribution. The major element composition measured in glass shards is typically a high-silica rhyolitic composition (Fig. 11C and Data S2: Table D). More specifically, two significantly different compositions can be identified. One corresponds to the layer at 600 to 604 cm bsf in the core MD18-3531 (for which the estimated age is approximately 30 ka BP, the early MIS 2 after the $\delta^{18}O$ curve interpretation, see Fig. 10); the other corresponds to the seven samples collected from the layers at 1075 to 1115 cm bsf in the core MD18-3530 and at 1495 to 1699 cm bsf in the core MD18-3531 (for which the estimated ages are about 100 ka BP, the middle MIS 5 after the $\delta^{18}O$ curve interpretation, see Fig. 10). The chemical composition of the glass shards from these latter two layers is similar for both major and trace elements. These similar compositions and textures argue in favour of the same origin for these two tephra

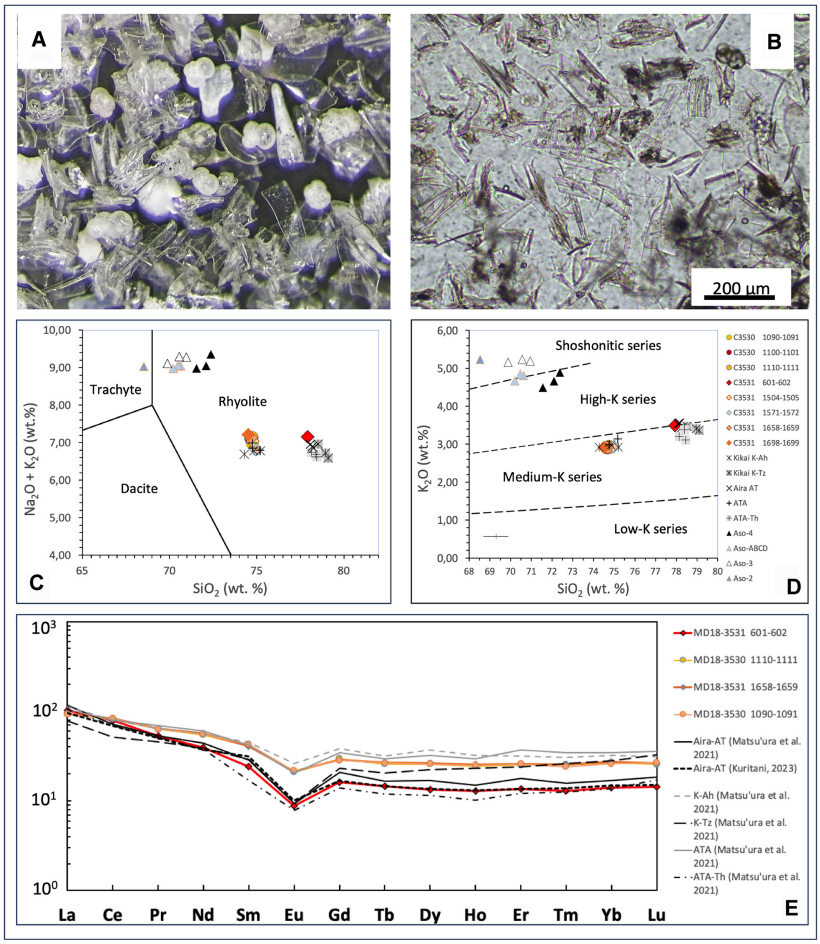

Fig. 11. Characterisation of tephra deposits: (A) Close-up image of typical volcanic glass shards (with foraminifera) in the sample MD18-3531 (1658 to 1659). (B) Microphotograph of the MD18-3530 (1090 to 1091) tephra layer. (C) Total alkalis versus silica plot (TAS; with classification based on Le Maitre *et al.*, 2002—same legend as Fig. 11D). (D) K_2O versus SiO_2 glass composition of MD18 tephra, compared to some distal tephra related to the volcanism of the Ryukyu-Kyushu arc (from Tsuji *et al.*, 2018; Matsu'ura *et al.*, 2021; Matsu'ura & Ueno, 2022). Error bars are 1σ std dev. (E) Chondrite-normalised (McDonough & Sun, 1995) REE patterns for some representative samples of the MD18 volcanic glass shards, with reference to compositions for some near-source large magnitude eruption deposits from the literature (Matsu'ura *et al.*, 2021; Kuritani, 2023).

layers. This is confirmed by isotopic analyses (Sr, Nd, Hf, Pb) carried out on these same layers (Data S2, Table E). Samples from the layer 1075 to 1115 in core MD18-3530 and from the layer 1495 to 1699 in MD18-3531 yield the same isotopic ratios and define a very restricted range for Sr-Nd-Hf-Pb isotopic systems. They probably have been emitted by the same volcanic eruption. The sample from the layer 600 to 604 in the core MD-18-3531 shows a significantly distinct isotopic signature attributed to a different volcanic eruption.

With regard to the potential volcanic sources in the area (e.g. Chen *et al.*, 1990; Mukasa *et al.*, 1994; Arakawa *et al.*, 1998; Hickey-Vargas, 1998; Shinjo *et al.*, 1999, 2000; Shinjo & Kato, 2000; Lai *et al.*, 2017; Li *et al.*, 2018; Fang *et al.*, 2019; McCarthy *et al.*, 2019; Heywood *et al.*, 2020; Kuritani, 2023), the Sr-Nd-Pb-Hf isotope results support that MD18-tephra originates from two distinct volcanic eruptions in the Ryukyu-Kyushu arc (Data S2: Fig. S2). For example, MD18 samples show strong similarities in terms of Sr-Nd-Pb-Hf isotopes with samples 'U1438' from the dataset of the paper of McCarthy *et al.* (2019) that are considered to come from the Ryukyu-Kyushu arc.

Several deep-water tephra layers could potentially be found to the east of the island of Taiwan (e.g. Machida, 2002). They are the product of large-volume silicic eruptions known in southern Kyushu and the Ryukyu-Kyushu arc, in particular some of the Quaternary eruptions that led to the formation of calderas, such as Kikai, Aira, Aso and Ata (e.g. Shinjo *et al.*, 2000). Our data are compared with those (e.g. Arakawa *et al.*, 1998; Shinjo *et al.*, 1999, 2000; Kimura *et al.*, 2015; Albert *et al.*, 2019; McLean *et al.*, 2020; Matsu'ura *et al.*, 2021; Matsu'ura & Ueno, 2022; Kuritani, 2023) obtained for large magnitude rhyolitic eruptions that produced distal tephra over the last 250 kyr in the Ryukyu-Kyushu district: Kikai-Akahoya (K-Ah, 6.3 ka), Aira-Tanzawa (AT, 21 to 25 ka), Aso 4

(70 to 90 ka), Kikai-Tozurahara (K-Tz, 75 to 95 ka), Ata (85 to 105 ka), Aso 3 (105 to 125 ka) and Ata-Torihama (Ata-Th, 230 to 250 ka).

From major elements, two compositional groups, with medium to high-K compositions and comprising our samples, can be clearly distinguished. A third group, richer in K_2O with lower SiO_2 contents, determined by tephra from Aso volcano, is compositionally distinct (Fig. 11C, 11D and Data S2: Fig. S1C). A good correlation exists between the published data for the AT (Aira), K-Tz (Kikai) and Ata-Th (Ata) deposits and our MD18-3531/601-602 cm sample. Trace element and isotopic data (Data S2: Tables D and E, Fig. S1D) clearly show that the best match is obtained with the AT (Aira) deposit data, in particular with the recent data from Kuritani (2023) for the three eruptive phases of this eruption sampled around the Aira caldera (Fig. 11E and Data S2: Fig. S2). The agreement, both in terms of age (30 009 ± 189 ka cal BP – Smith *et al.*, 2013; Albert *et al.*, 2019), and geochemical and textural parameters, leads us to interpret the MD18 tephra layer (600 to 604 cm) as originating from the Aira-Tanzawa (AT) eruption.

The seven glass shard samples collected from layers at 1075 to 1115 cm bsf in the core MD18-3530 (three samples) and at 1495 to 1699 cm bsf in the core MD18-3531 (four samples) show identical compositions for major and trace elements, as well as for Sr-Nd-Hf-Pb isotopes, suggesting that they originate from the same volcanic event. Major and trace element values (Fig. 11 and Data S2) are close to those published for tephra K-Ah (Kikai) and Ata (Ata caldera), but K-Ah is from a very recent eruption (~7 kyr – Tsuji *et al.*, 2018; McLean *et al.*, 2018), which cannot correspond to the MD18-3530 (1075 to 1115 cm) and MD18-3531 (1495 to 1699 cm) layers. Furthermore, isotopes do not support a provenance from the eruption of the Kikai caldera. Consequently, the volcanic particles of these layers must come from the Ata eruption, with an age of ~100 kyr.

DISCUSSION

Hemipelagic sedimentation rates

Average hemipelagic sedimentation rates calculated based on radiocarbon dating, isotopic stratigraphy, tephrostratigraphy and finally by the analysis of ^{230}Th excess in the upper layers of the boxcores are consistent, ranging from 3 cm/kyr to 8 cm/kyr.

Hemipelagic sedimentation is supposed homogeneous at the scale of the study area. Nayak *et al.* (2021) have shown a high content of smectite, both in hemipelagic sediment and turbidites of the Hateruma basin, indicating that it is consistent with a sediment source from the Ryukyu Islands with a contribution of suspended clays transported from the Luzon Arc in the south *via* the Kuroshio Current (Nayak *et al.*, 2021; Garzanti *et al.*, 2023). This contribution could be higher during the glacial period with the possible deviation of a part of the mainstream of the Kuroshio Current above the study area and amplified by the increase in primary productivity during the late Glacial Maximum (Fenies *et al.*, 2023).

Minimum hemipelagic sedimentation rates were obtained using radiocarbon data on the sites MD18-3530 and MD18-3531, with the lowest values (3 cm/kyr) during the Holocene time. These results are consistent with the values calculated for the cores RN87-PC4 from Xu & Ujiie (1994) and YK15-0PC13 from Kanamatsu *et al.* (2020), respectively about 3.2 cm/kyr and 3.8 cm/kyr over the last 100 kyr.

Over the last 20 kyr, hemipelagic sedimentation rates are estimated to be higher in MD18-3528 and MD18-3529 than in MD18-3530 and MD18-3531, with values around 7–8 cm/kyr. This difference can be due to a higher contribution of detrital clay in a context where numerous thick turbidites are observed. Uncertainties in identifying the end of turbidites and the beginning of true hemipelagic sedimentation are high and can also explain the overestimation of hemipelagic thickness.

Sediment source of gravity-flow processes

Most sandy turbidites are composed of bioclastic sand dominated by planktonic foraminifera tests. In the finest intervals (fine-sand and silt), the composition is mixed with small foraminifera and small-size calcareous debris, siliceous tests, quartz, feldspars and other metamorphic grains. The clayey component has a similar composition to that in hemipelagic layers, which indicates a common source for detrital clay sediments despite different depositional processes (Nayak *et al.*, 2021). The sediment source for turbidites is mainly marine accumulations, from the Ryukyu shelf to the submarine slope. It is dominated by biogenic carbonate, as is most of

the shelf to upper slope sediments (Tsuji, 1993). The detrital component of fine-grained sediments is compatible with a sediment source from the erosion of the Ryukyu Islands. The morphological analysis of the seafloor supports that most of the turbidity currents are generated on the northern slope of the basin and follow the canyon and gully axis (Fig. 2).

The mini-basin in the outer-arc high is isolated most of the time from sediment sources coming from the islands. Turbidity currents should have a local source from the available sediment around the mini-basin. Only exceptional ones could flow through the 3200 m bsl deep pass northeast of the mini-basin (Fig. 2). The discrimination of muddy turbidites and hemipelagic deposits in the mini-basin (MD18-3531 site) is particularly complex because of the similar composition. Except for volcanic ash, most turbidites are composed of reworked marine material. Turbidites are thick in the mini-basin (MD18-3531), compared to those described in MD18-3530. The narrowness of the floor of the mini-basin induces a confining effect and a vertical stack of all the sediments transported by the turbidite flows on a small surface.

The most significant mass-transport deposits are located on the gentle slope of the Hateruma basin seafloor. In MD18-3530, the two thickest debrites are entirely muddy, with a muddy matrix containing mud clasts. They probably correspond to gravity instabilities occurring on the submarine slope of the northern side of the Hateruma basin. In contrast, the most recent debrite contains coarse calcareous debris (blocks and gravels) coming from the coral reef area. The source of this deposit must be from the Sakisei-Shoko reef-lagoon, also corresponding to the location of the head of the largest submarine canyon (Kuroshima Canyon in Fig. 2). After Ikehara *et al.* (2022), most of the carbonate sands from the shallower area through the Kuroshima submarine canyon were deposited on a small submarine fan at the canyon mouth. This work shows that the largest submarine gravity flows probably extend deeper into the Hateruma basin.

The sediments of the mega-deposits are mixed. Carbonates are present in the sandy fractions, while the fractions of very-fine sand and silt show a terrigenous source. The large volumes of muddy sediment in the homogenite interval show an average magnetic susceptibility lower than that of pelagic sedimentation (Fig. 6). This is probably a well-sorted mixture of the finest particles of marine platform and upper-slope sedimentation containing detrital clays and carbonate mud. The source of these sediments is thought to be a regional re-suspension of platform and upper slope sediments, probably linked to a very large tsunami, similar to that observed, for example, in the Ionian Sea (San Pedro *et al.*, 2017).

Reworked tephra layers

The identification of the origin of both tephra layers is based on age models and geochemical analysis. The source of the volcanic sediments and the eruptions is identified from two volcanoes located to the south of Kyushu: Aira eruption (30 ka BP) and Ata eruption (100 ka BP). The distance of the two volcanoes from the study area exceeds 1000 km. The Ata deposit was previously described in the Hateruma area by Xu & Ujiie (1994) and by Kanamatsu *et al.* (2020) but with a thickness of about 10 cm. The Ata deposit, 40 and 200 cm thick respectively identified in MD18-3530 and MD18-3531, is unexpected. The description of laminations, successive normal grading layers and the presence of various quantities of foraminifera in the different layers lead to interpreting these deposits as reworked tephra by gravity-flow processes on the seafloor. However, the breakable characteristic of the volcanic particles (vesiculated glasses) and their high concentration (reaching locally 80%) indicate that this secondary transport was probably short. The rapid loading of the submarine slopes by volcanic particles due to the primary tephra accumulation increased the potential for slope instability, especially in the steepest slopes. Turbidity currents could be triggered either at the time of primary deposition or during a low- or medium-intensity earthquake after this deposition. The 2 m thick accumulated tephra layer in the mini-basin could be the result of multiple turbidity currents triggered around the basin flanks and the stacking of the transported sediment in the very narrow basin floor.

The identification of the Aira deposit (30 ka BP) is new in this area. It was not observed in the previous cores collected near the Hateruma area. The extension of this deposit was initially limited to about 500 km of the study area, in the work of Matsu'ura *et al.* (2021) based on coring data collected south of Japan. In the core MD18-3531, the process of concentration and stacking

of the volcanic particles by low-density turbidity currents has facilitated the detection of this tephra layer.

Correlation of gravity-flow deposits

A stratigraphic correlation of the four cores is proposed in Fig. 12. The core KR15-PC03 published by Ikehara *et al.* (2022) is added to the correlation panel, completing the dating and the description of facies evolution. The correlation of individual gravity-flow deposits was possible by integrating all the stratigraphic data: radiocarbon dating, ^{18}O stratigraphy, tephrochronology and physical correlation based on the interpretation of Chirp profiles (Fig. 3). Given the low resolution of the isotopic stratigraphy and the limited number of radiocarbon ages, it was not possible to calculate sufficiently accurate age for each turbidite. The attempt to provide age ranges in Data S4 is indicative but does not allow for all uncertainties to be considered, particularly erosion. It can only be used as a guide. Uncertainties of the age models are too high to propose a reliable correlation only based on the age model. The correlation proposed in Fig. 12 considers all the established chronostratigraphic constraints and is then based on the number of deposits and the stacking pattern of turbiditic deposits.

Four mega-events, named from ME1 (the youngest in MD18-3528) to ME4 (the oldest in MD18-3531), are defined by the occurrence of a mega-deposit in one of the cores. They also correspond to the four mega-deposits MD1 to MD4, described in the cores (Figs 6 and 7). In the chrono-stratigraphic framework, mega-deposits are laterally correlated with debris-flow deposits in MD18-3530, or sandy turbidites in KR15-PC03 or MD18-3531 (orange in Fig. 12).

The Aira tephra layer (purple in Fig. 12), dated at 30 ka BP, is only described in MD18-3531 below

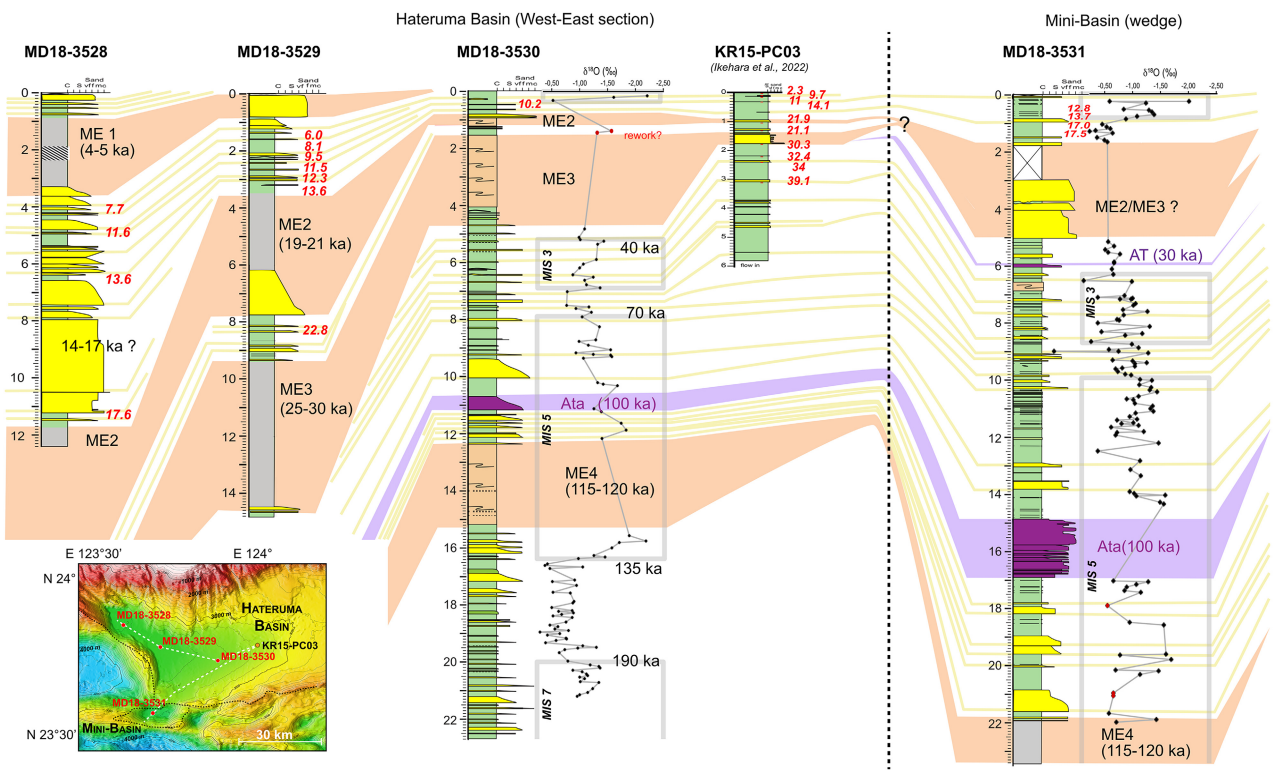

Fig. 12. Correlation panel of five cores: MD18-3528, MD18-3529, MD18-3530, KR15-PC03 (from Ikehara *et al.*, 2022) across the Hateruma basin, and MD18-3531 collected in the mini-basin at the top of the accretionary wedge (location on the map). Correlations are based on radiocarbon dating, geometry of mega-deposits provided by Chirp echo-sounder profiles, tephra identification and $\delta^{18}O$ stratigraphy for MD18-3530 and MD18-3531. Orange areas for mega-deposits (including thick sandy turbidites), yellow lines for turbidite sequences, purple areas for tephra layers. Radiocarbon ages are indicated in red and approximated ages in black.

the base of the mega-event ME3. It is probably eroded by ME3 at the MD18-3530 site.

The correlation panel (Fig. 12) underlines the strong contrast of total sedimentation rates, number and thickness of gravity-flow deposits in the deep part of the basin (MD18-3528 and 3529) and in the other sites. Gravity-flow deposits dominate all core sites with sedimentation rates from 2 to 10 times higher than the hemipelagic rate (3–8 cm/kyr).

Thick sandy deposits are confined in the deepest part of the basin (MD18-3528) and pinch out laterally with thin sandy layers in MD18-3529 and often no equivalent turbidite in the other cores. Despite uncertainties of the stratigraphic framework, especially with the resolution of the $\delta^{18}O$ curves, the same number of gravity-flow deposits is identified in the stratigraphic interval 0 to 120 ka BP in MD18-3530 and MD18-3531 cores. Based on physical properties (magnetic susceptibility) and chemical curves (Ca, Fe curves and Zr/Rb ratio), almost all the individual turbidites are correlated in both grain size and relative thickness. The largest differences are: (1) the sedimentary facies for the mega-events correspond to a debrite in MD18-3530 and to sandy turbidites in MD18-3531; and (2) the strong thickening of the sedimentary succession between the Ata tephra and the mega-event ME4 in the core MD18-3531.

Number and types of gravity-flow events

The number of submarine gravity-flow deposits for each core is: 25 deposits for the last 20 kyr for MD18-3528, 21 deposits for the last 30 kyr for MD18-3529, 49 deposits for the last 200 kyr for MD18-3530 and 36 deposits for the last 120 kyr for MD18-3531.

The frequency of gravity-flow deposits varies spatially in the study area, with a significant increase in the number of gravity flows reaching the deepest part of the Hateruma basin. It is an efficient trap for the gravity flows coming from the shelf and the slope. Both MD18-3529 and 3530 cores are located shallower in the eastern part of the basin, and many gravity-flow deposits recorded in MD18-3528 do not reach them. The triggering zone of the gravity flows could extend along all the northern side of the Hateruma basin. From a mineralogical point of view (clays and sandy-silty minerals), the detrital content of the turbidites is consistent with products of erosion from the Ryukyu Islands. The canyon network located at the northwest of the Hateruma basin is probably a major source of sediment. Most of the gravity flows remain trapped in the basin floor and correspond to gravity-flow events with a local extension (type-1 event in Fig. 13).

Gravity flow deposits identified in cores MD18-3530 and MD18-3531 and possibly correlated between all cores can be considered large regional gravity-flow events. The correlation between events at two morphologically independent sites (Hateruma Basin and the small basin of MD18-3531) indicated that turbidites were probably generated by multiple simultaneous turbidity currents in the Hateruma Basin (in different canyons of the northern slope) and in small basins of the outer-arc high (type-2 event in Fig. 13). The triggering of these large multi-source gravity-flow events could be great subduction earthquakes, as it was shown in other areas in the world (Goldfinger, 2011 and references therein).

The largest gravity-flow events recorded in the study area are the mega-events (or type-3 event in Fig. 13). They correspond to thick deposits showing different sedimentary facies (debris-flow deposits, mega-deposits with homogenite or thick turbidites in Fig. 12), indicating different gravity-flow processes related to the core location (basin floor, base of slope…). It also indicates multiple simultaneous triggering of gravity flows, with a large volume of re-suspended muddy sediment. The frequency of these largest events is low, with only four events identified in the last 200 kyr. The age estimations of the four mega-events are about: 4 to 5 ka BP for ME1, 18 to 20 ka BP for ME2, 25 to 30 ka BP for ME3 and 115 to 120 ka BP for ME4 (Fig. 12).

The sedimentary facies of mega-deposit with a thick homogenite interval is generally associated with great tsunamis, especially in the Mediterranean Sea where the basins are closed (Cita *et al.*, 1996; San Pedro *et al.*, 2017). They have also been described in large subduction zones, such as Caribbean (Seibert *et al.*, 2024), and East Japan (McHugh *et al.*, 2016, 2020; Strasser *et al.*, 2024). The thickness of the homogenite layer seems to be related to the size, the confinement degree of the basin (sink morphology) and the volume of supplied mud. In most cases, the origin of large volumes of muddy sediment re-suspended in the water column is debated. It could come from the re-suspension of muddy sediment from the shelf areas by large tsunami waves (San Pedro *et al.*, 2017), or from the widespread entrainment of surficial sediments by the

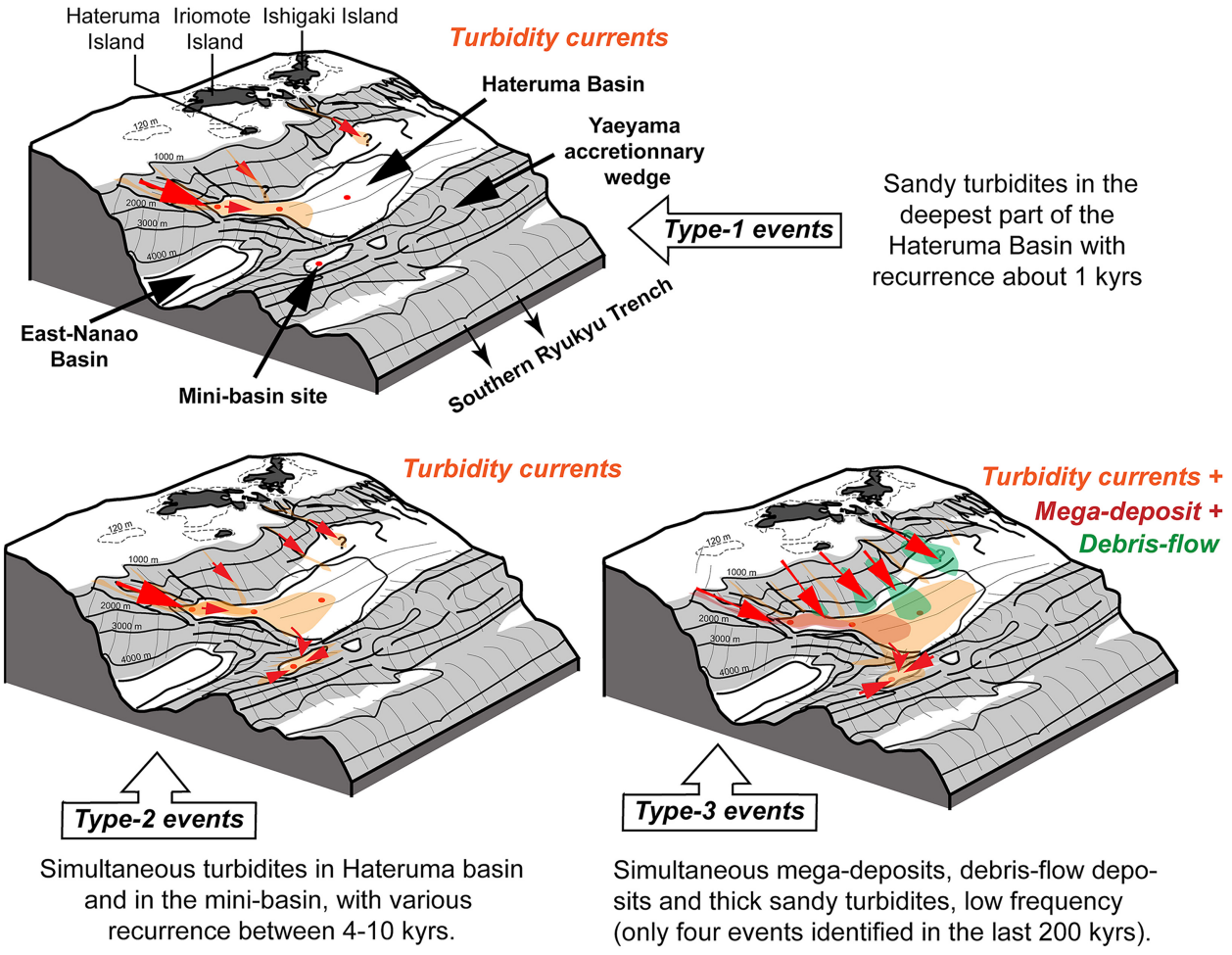

Fig. 13. Synthetic view of the three types of large gravity event recorded in the deep-marine sedimentary deposits of the Hateruma area (dark grey for the islands, light grey for the steep submarine slope, white for platform and basin floor).

low frequency and long duration motions of earthquake rupture on subduction megathrusts, as shown by McHugh *et al.* (2020). The settling of these large volumes of mud leading to low-density gravity flows on the submarine slopes concentrates the fine and sorted sediments at the bottom of the basin, forming thick homogenous deposits.

Event recurrences

The chronology of gravity-flow events is reported in Fig. 14 for each core. The given ages were determined with radiocarbon ages for the last 20 kyr, considering hemipelagic sedimentation rates and hemipelagic thicknesses between gravity-flow deposits (see Data S4). Due to high uncertainties of age models, most events are represented with an average time interval of 1000 years for the last 20 kyr (Fig. 14A) and do not fit perfectly from one sediment core to another. The recurrence intervals of gravity-flow events vary significantly, from several centuries to over 4000 years. They vary from site to site, but also in time. For example, in MD18-3528, the average recurrence is about 1000 years during the last 11 kyr and is about 600 years between 11 and 20 ka BP (Fig. 14A).

The comparison of the tsunami records in the coastal areas of the Yaeyama Islands (Kawana & Nakata, 1994; Ando *et al.*, 2018) with the gravity events observed in MD18-3528 shows a consistent number of events over the last 5000 years. The dating of coastal tsunami deposits also has

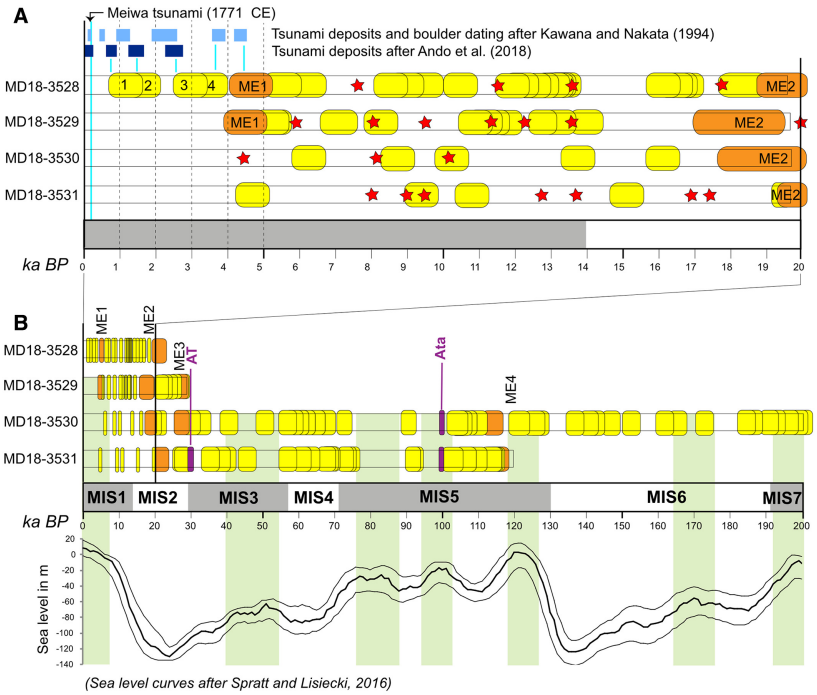

Fig. 14. (A) Chronological diagram of the gravity deposits identified in the four sediment cores MD18-3528, MD18-3529, MD18-3530, and MD18-3531 (including Calypso and boxcore data) during the last 20 kyr; yellow boxes correspond to turbidite deposits, orange boxes correspond to mega-events, and red stars are the locations of radiocarbon dating. The upper part reports the dating of paleo-tsunamis after the studies of Kawana & Nakata (1994) and Ando *et al.* (2018). (B) Chronological diagram of the gravity deposits identified in the studied cores during the last 200 kyr. The ages of turbidites are approximated using the $\delta^{18}O$ curves, the tephra identification (purple), the correlation between cores MD18-3530 and MD18-3531, and the mean sedimentation rates. Each turbidite covers 5000 years for each event. Obtained data are compared to the global curve of sea-level variations given by Spratt & Lisiecki (2016) surrounded by 2-sigma uncertainty. Green bands underline relative highstands in correlation with periods of low occurrence of gravity events.

relatively large uncertainties (about 300 to 600 years). However, no submarine gravity-flow deposit has been identified during the last centuries, excluding the record of the Meiwa tsunami of 1771 CE at the core sites. The tsunami deposits studied by Ando *et al.* (2018) provided a record of four tsunamis in the last 3000 years, and the work of Kawana & Nakata (1994) showed a series of six tsunami records with recurrence intervals between 400 and 1200 years over the last 5000 years (Fig. 14A). Except for the Meiwa tsunami, the five other events could be consistent with the last five gravity-flow events recorded in MD18-3528, including the most recent mega-event ME1 dated between 4500 and 5000 years BP (Fig. 14A). The submarine gravity-flow deposits of MD18-3528 could constitute another possible sedimentary record of large events associated with large tsunamis for the last 20 kyr, with recurrence intervals ranging between 600 and 1000 years. The events that trigger the turbidity currents may not be directly the tsunamis but could also be the earthquakes that generated tsunamis. The absence of any record of the Meiwa tsunami at the four core sites suggests that the origin of this tsunami (submarine landslide or major earthquake) was sufficiently distant from the Hateruma basin to not have generated any significant submarine gravity processes down to the basin floor.

At the sites MD18-3530 and 3531, the average recurrence intervals of gravity-flow events are about 3500 to 4000 years (Fig. 14A). Only the largest events affecting a large part of the submarine slope of the Hateruma area are recorded, also including the mini-basin of the Yaeyama ridge (mostly type-2 events). At a longer time scale (Fig. 14B), cores MD18-3530 and 3531 provide sedimentary records of these strong-

intensity events over the last 200 kyr. With large chronostratigraphic uncertainties, the events are represented in Fig. 14B on an average time interval of 5000 years. The average recurrence periods of gravity-flow events are calculated at 3800 years for MD18-3530 (for 200 kyr) and 3600 years for MD18-3531 (for 120 kyr). However, the frequency of these great events is variable in time, and this variability seems consistent in the two cores, showing a series of close events separated by periods of rest.

The frequency of mega-events (type-3 event) is low with only four events identified over the last 200 kyr. It corresponds to the largest gravity-flow events (major slope instabilities), which were probably associated with huge tsunamis, considering the high volume of re-suspended sediments, but the origin of the exceptional size of the deposit is still unclear. Two are identified around 20 to 30 ka BP during the last low sea-level.

Possible impact of sea-level variations

The periods of gap or low-frequency events are marked with light green bands in Fig. 14B and compared with the global sea-level curve (Spratt & Lisiecki, 2016). The correlation with the relative high sea-levels during the last 150 kyr seems clear, indicating a control of the sea-level on the ability to generate great submarine slope instabilities. During high sea-level periods, the platform is submerged, allowing carbonate reefs to develop. This platform is subject to dissolution and erosion during sea-level lowstands, inducing more sediment transfer toward the upper slope. Moreover, the impact of tsunami was stronger at the shelf break during low sea-level periods, re-suspending sediments and directly generating gravity instabilities by hitting the top of the upper submarine slope and the canyon heads. In addition, in their study, Fenies *et al.* (2023) showed that the Kuroshio Current could be partly deviated along the Ryukyu forearc basins during glacial stages (Fenies *et al.*, 2023), inducing higher sedimentation rates due to an increase of clay minerals transported in suspension in the current and an increase of biological primary productivity (Fenies *et al.*, 2023). With higher sediment load and the emersion of a part of the platform, the submarine slope becomes more responsive to gravity instabilities in conditions of low sea-level. Considering these changes in the sedimentary context, the sedimentary record of great events such as earthquakes and tsunamis in deep-sea environments could be influenced by sea-level variations.

CONCLUSIONS

The Hateruma forearc basin, located in the southern part of the Ryukyu subduction zone, is dominated by the sedimentation of gravity-flow deposits, with sediment coming from the shelf and submarine slope, south of the Yaeyama Islands. New coring data provide access to a long-term sedimentary record (up to 200 000 years) of major submarine gravity-flow events in the deep marine area of the Hateruma basin.

Thanks to a combination of stratigraphic and dating methods, including radiocarbon dating, U and Th-series nuclides analysis, $\delta^{18}O$ stratigraphy and tephrochronology, a stratigraphic model was established for each core and boxcore ranging from the last few centuries to several hundred thousand years. Sedimentological and chrono-stratigraphic data allowed identification and approximated dating of the submarine gravity-flow deposits and their correlation between the different core sites in the Hateruma basin and in an isolated mini-basin at the top of the accretionary wedge.

The deep basin floor of the Hateruma basin is an efficient trap for submarine gravity flows, with high bulk sedimentation rates exceeding 60 cm/ka, and twenty-four gravity-flow deposits over the last 20 000 years. Further east, on the gently sloping side of the basin, bulk sedimentation rates and the number of gravity-flow deposits dropped from 5 to 10 cm/ka and forty-eight gravity-flow deposits respectively over the last 200 000 years (i.e. five times fewer per time interval).

Three types of gravity-flow events are identified:

1 High-density turbidity currents (sandy turbidites) affecting only the deepest part of the Hateruma basin, with a recurrence time of about 1000 years. The chronology of these events is consistent with the major tsunamis recorded on land on the Yaeyama Islands during the last 5000 years. The events that trigger the turbidity currents may not be directly the tsunamis but could also be the earthquakes that generated tsunamis. No sedimentary record of the last historical Meiwa tsunami (1771 CE) is identified in the four cores. It suggests that the source of this

historical tsunami was probably distant from the Hateruma basin, whether it was triggered by a submarine landslide or an earthquake.

2 Regional turbidity currents simultaneously recorded at the four coring sites (including at the top of the accretionary wedge), with a recurrence time of around 3500–4000 years; these events could correspond to major seismic events, mega-earthquake ($M > 7$) linked to the subduction process.

3 Mega-events including synchronous debris-flow deposits, mega-deposits with homogenite facies and thick sandy turbidites. For this third type of thick deposits, only four events have been identified over the last 200 000 years, and from a sedimentary point of view, the origin of these exceptionally large events is still unclear. They correspond to major destabilisations of the submarine slope on the scale of the Hateruma basin, and the sedimentary facies are compatible with the re-suspension of fine sediments associated with major tsunamis.

The frequency of the large gravity-flow events increases during periods of low sea-level. The destabilisation of the upper slope sediments is probably favoured by the emersion of a large part of the shelf. Instability of the slope could also be amplified by higher marine sedimentation rates toward the study area during glacial periods.

This work provides an unprecedented record of the different types of major submarine gravity instabilities and their frequencies, which in an active subduction context are linked to the activity of major faults that control the entire structure and morphology of this submarine slope. Although their recurrence periods inferred from this study are long (millennia), mega-earthquakes and tsunamis must be considered in the evolution of the subduction segments where instrumental seismicity is currently low to moderate.

ACKNOWLEDGEMENTS

We thank the captain, the crew, the technical team and onboard scientists and students of the French research vessel Marion Dufresne during the MD214/EAGER Cruise. We also thank the French Research Institution, that is, the French Oceanographic Fleet (FOF), IFREMER, GENAVIR, CNRS and the French Universities associated with the EAGER project. Great thanks to Taiwanese support of TORI (Taiwan Oceanographic Research Institute), IO-NTU (Institute of Oceanography – National Taiwan University) and NCU (National Central University). Funding for analysis was provided by different projects and institutions: LIA CNRS D3E and IRP CNRS G2E, INSU projects (Tellus-Postcampagne 2019, Tellus-Aleas 2020, INSU ARTEMIS program for AMS radiocarbon dating). This work was supported by the ISblue project, Interdisciplinary graduate school for the blue planet (ANR-17-EURE-0015) and co-funded by a grant from the French government under the programme 'Investissements d'Avenir' embedded in France 2030. This is Contribution N°715 of the ClerVolc Program of Excellence of the International Research Centre of Disaster Sciences and Sustainable Development of the University Clermont Auvergne. For the geochemical analysis, we also thank F. Dewilde, PSO Brest for $\delta^{18}O$ measurements, J.-L Devidal (LMV) for EPMA and LA-ICP-MS analysis. S. Dominguez is warmly thanked for obtaining a very high-quality bathymetric background from data of extremely disparate resolutions.

List of other participants of EAGER Cruise: Aizawa M, Ballas G., Chang J.-H., Chang Y.-P., Chen T.-T., Chen Y.-H., Das P., Degeai J.-P., Déverchère J., De Raco O., Gosset N., Herlédan M., Ho S.-L., Hsu H.-H., Huang Y.-S., Lanson M., Letourneau C., Lin H.-S., Lin L.-F., Lin L.-K., Longo M., Mérindol M., Mercier de Lépinay B., Miramontes E., Morena P., Nayak K., Oregioni D., Patry L., Pillutla R. K., Rigalleau V., San Pedro L., Su P.-J., Volage F., Wei K.-Y., Whilhelm B., Yu N.-T., Yu P.-S.

AUTHOR CONTRIBUTIONS

NB is the Principal Investigator of the EAGER project. She was responsible for acquiring the data, and for processing and interpreting the data presented in this article. She supervised the students, who carried out sedimentological analyses and data interpretation. She produced a large part of the figures and wrote most of the text. GR and SL are the two main collaborators behind the project. They participated in interpreting, discussing the data, writing and improving the text. CG and MR acquired most of the sedimentological and stratigraphic data ($\delta^{18}O$ and radiocarbon) on the sediment cores and participated in interpretation of the data. MC has produced the analyses, with the help of CG and interpreted the

data on U and Th-series. He wrote this section and Supporting Information on these data. DB and PB have acquired the data, interpreted the results of petrological and geochemical analyses of tephra. SKH, CCS, RS, TSL, MAB, MR and AC all participated in the development of the scientific project, the EAGER oceanographic cruise, the strategy for the coring targets and the scientific discussion of the data. Their contributions were essential to the completion of this article, with their help in improving the manuscript. EAGER Scientific Team is the entire scientific team on board the R/V Marion Dufresne for the processing of sediment cores.

CONFLICT OF INTEREST

We declare that we have no commercial or associative aim that might represent a conflict of interest in connection with the work submitted.

DATA AVAILABILITY STATEMENT

The original contributions presented in the study are included in the article and in the Supporting Information. The data that support the findings of this study (including core photographs, XCT images, MSCL and XRF data, laser granulometry measurements) is available in SEANOE (SEA scieNtific Open data Edition) repository at doi: 10.17882/108294, reference number 108294.

REFERENCES

Albert, P.G., **Smith, V.C.**, **Suzuki, T.**, **McLean, D.**, **Tomlinson, E.L.**, **Miyabuchi, Y.**, **Kitaba, I.**, **Mark, D.F.**, **Moriwaki, H.**, **SG06 Project Members** and **Nakagawa, T.** (2019) Geochemical characterisation of the Late Quaternary widespread Japanese tephrostratigraphic markers and correlations to the Lake Suigetsu sedimentary archive (SG06 core). *Quat. Geochronol.*, **52**, 103–131.

Anderson, R.F., **Bopp, R.F.**, **Buesseler, K.O.** and **Biscaye, P.E.** (1988) Mixing of particles and organic constituents in sediments from the continental shelf and slope off Cape Cod: SEEP-1 results. *Cont. Shelf Res.*, **8**, 925–946.

Ando, M., **Kitamura, A.**, **Tu, Y.**, **Ohashi, Y.**, **Imai, T.**, **Nakamura, M.**, **Ikuta, R.**, **Miyairi, Y.**, **Yokoyama, Y.** and **Shishikura, M.** (2018) Source of high tsunamis along the southernmost Ryukyu trench inferred from tsunami stratigraphy. *Tectonophysics*, **722**, 265–276.

Arai, R., **Takahashi, T.**, **Kodaira, S.**, **Kaiho, Y.**, **Nakanishi, A.**, **Fujie, G.**, **Nakamura, Y.**, **Yamamoto, Y.**, **Ishihara, Y.**, **Miura, S.** and **Kaneda, Y.** (2016) Structure of the tsunamigenic plate boundary and low-frequency earthquakes in the southern Ryukyu Trench. *Nat. Commun.*, **7**, 12255.

Arakawa, Y., **Kurosawa, M.**, **Takahashi, K.**, **Kobayashi, Y.**, **Tsukui, M.** and **Amakawa, H.** (1998) Sr–Nd isotopic and chemical characteristics of the silicic magma reservoir of the Aira pyroclastic eruption, southern Kyushu, Japan. *J. Volcanol. Geotherm. Res.*, **80**, 179–194.

Araoka, D., **Inoue, M.**, **Suzuki, A.**, **Yokoyama, Y.**, **Edwards, R.L.**, **Cheng, H.**, **Matsuzaki, H.**, **Kan, H.**, **Shikazono, N.** and **Kawahata, H.** (2010) Historic 1771 Meiwa tsunami confirmed by high-resolution U/Th dating of massive Porites coral boulders at Ishigaki Island in the Ryukyus. Japan. *Geochem. Geophys. Geosyst.*, **11**, Q06014.

Araoka, D., **Yokoyama, Y.**, **Suzuki, A.**, **Goto, K.**, **Miyagi, K.**, **Miyazawa, K.**, **Matsuzaki, H.** and **Kawahata, H.** (2013) Tsunami recurrence revealed by Porites coral boulders in the southern Ryukyu Islands, Japan. *Geology*, **41**, 919–922.

Argus, D.F., **Gordon, R.G.** and **DeMets, C.** (2011) Geologically current motion of 56 plates relative to the no-net-rotation reference frame. *Geochem. Geophys. Geosyst.*, **12**, 458.

Babonneau, N. and **Ratzov, G.** (2018) MD 214/EAGER cruise, RV Marion Dufresne. https://doi.org/10.17600/18000520.

Beck, C., **Reyss, J.L.**, **Leclerc, F.**, **Moreno, E.**, **Feuillet, N.**, **Barrier, L.**, **Beauducel, F.**, **Boudon, G.**, **Clément, V.**, **Deplus, C.**, **Gallou, N.**, **Lebrun, J.-F.**, **Le Friant, A.**, **Nercessian, A.**, **Patrene, M.**, **Pichot, T.** and **Vidal, C.** (2012) Identification of deep subaqueous co-seismic scarps through specific coeval sedimentation in Lesser Antilles: implication for seismic hazard. *Nat. Hazards Earth Syst. Sci.*, **12**, 1755–1767.

Boudreau, B.P. (1994) Is burial velocity a master parameter for bioturbation? *Geochim. Cosmochim. Acta*, **58**, 1243–1249.

Chase, Z. (2008) Sediment signatures of U- and Th-series nuclides and their application as paleoceanographic tracers. In: *U-Th Series Nuclides in Aquatic Systems* (Eds Krishnaswami, S. and Cochran, J.), pp. 383–416. Elsevier, London.

Chase, Z., **Anderson, R.F.**, **Fleisher, M.Q.** and **Kubik, P.W.** (2003) Scavenging of ^{230}Th, ^{231}Pa and ^{10}Be in the southern ocean (SW Pacific sector): The importance of particle flux, particle composition and advection. *Deep Sea Res. Part II Top. Stud. Oceanogr.*, **50**, 739–768.

Chen, Y.L. (2000) Comparisons of primary productivity and phytoplankton size structure in the marginal regions of southern East China Sea. *Cont. Shelf Res.*, **20**, 437–458.

Chen, G. and **Huang, R.** (2008) Influence of monsoon over the warm pool on interannual variation on tropical cyclone activity over the western North Pacific. *Adv. Atmos. Sci.*, **25**, 319–328.

Chen, J.H., **Edwards, R.L.** and **Wasserburg, G.J.** (1986) ^{238}U-^{234}U-^{232}Th in seawater. *Earth Planet. Sci. Lett.*, **80**, 241–251.

Chen, C.H., **Shieh, Y.N.**, **Lee, T.P.**, **Chen, C.H.** and **Mertzman, S.A.** (1990) Nd-Sr-O isotopic evidence for source contamination and an unusual mantle component under Luzon Arc. *Geochim. Cosmochim. Acta*, **54**, 2473–2483.

Chen, H.-Y., **Ikuta, R.**, **Hsu, Y.-J.**, **Tsujii, T.**, **Ando, M.**, **Tu, Y.**, **Kohmi, T.**, **Takemoto, K.**, **Mizuno, K.**, **Tung, H.**, **Ku, C.-S.** and **Lin, C.-H.** (2021) A Decade of Global Navigation Satellite System/Acoustic Measurements of Back-Arc Spreading in the Southwestern Okinawa Trough. *Front. Earth Sci.*, **9**, 601138.

Chen, H.-Y., **Hsu, Y.-J.**, **Ikuta, R.**, **Tung, H.**, **Tang, C.-H.**, **Ku, C.-S.**, **Su, H.-H.**, **Jian, P.-R.**, **Ando, M.** and **Tsujii, T.** (2022) Strain partitioning in the southern Ryukyu margin revealed by seafloor geodetic and seismological observations. *Geophys. Res. Lett.*, **49**, e2022GL098218.

Cita, M.B., **Camerlenghi, A.** and **Rimoldi, B.** (1996) Deep-sea tsunami deposits in the eastern Mediterranean: new evidence and depositional models. *Sediment. Geol.*, **104**, 155–173.

Covault, J.A. and **Graham, S.A.** (2010) Submarine fans at all sea-level stands: Tectono-morphologic and climatic controls on terrigenous sediment delivery to the deep sea. *Geology*, **38**, 939–942.

Dezileau, L., **Lehu, R.**, **Lallemand, S.**, **Hsu, S.K.**, **Babonneau, N.**, **Ratzov, G.**, **Lin, A.T.** and **Dominguez, S.** (2016) Historical reconstruction of submarine earthquakes using 210Pb, 137Cs, and 241Am turbidite chronology and radiocarbon reservoir age estimation off East Taiwan. *Radiocarbon*, **58**, 25–36.

Diekmann, B., **Hofmann, J.**, **Henrich, R.**, **Fütterer, D.K.**, **Rohl, U.** and **Wei, K.-Y.** (2008) Detrital sediment supply in the southern Okinawa Trough and its relation to sea- level and Kuroshio dynamics during the late Quaternary. *Mar. Geol.*, **255**, 83–95.

Dominguez, S., **Lallemand, S.**, **Malavieille, J.** and **Schnürle, P.** (1998) Oblique subduction of the Gagua Ridge beneath the Ryukyu accretionary wedge system: Insights from marine observations and sandbox experiments. *Mar. Geophys. Res.*, **20**, 383–402.

Doo, W.B., **Lo, C.L.**, **Wu, W.N.**, **Lin, J.Y.**, **Hsu, S.K.**, **Huang, Y.S.** and **Wang, H.F.** (2018) Strength of plate coupling in the southern Ryukyu subduction zone. *Tectonophysics*, **723**, 223–228.

Dou, Y., **Yang, S.**, **Liu, Z.**, **Clift, P.D.**, **Yu, H.**, **Berne, S.** and **Shi, X.** (2010) Clay mineral evolution in the Central Okinawa Trough since 28ka: implications for sediment provenance and paleoenvironmental change. *Palaeogeogr. Palaeoclimatol. Palaeoecol.*, **288**, 108–117.

Dou, Y., **Yang, S.**, **Liu, Z.**, **Shi, X.**, **Li, J.**, **Yu, H.** and **Berne, S.** (2012) Sr–Nd isotopic constraints on terrigenous sediment provenances and Kuroshio Current variability in the Okinawa Trough during the late Quaternary. *Palaeogeogr. Palaeoclimatol. Palaeoecol.*, **365**, 38–47.

Fang, X., **Zeng, Z.**, **Hu, S.**, **Li, X.**, **Chen, Z.**, **Chen, S.** and **Zhu, B.** (2019) Origin of pumice in sediments from the middle Okinawa trough: constraints from whole-rock geochemical compositions and Sr-Nd-Pb Isotopes. *J Mar Sci Eng*, **7**, 462.

Fenies, P., **Bassetti, M.A.**, **Riveiros, N.V.**, **Menniti, C.**, **Frigola, C.**, **Babonneau, N.**, **Ratzov, G.**, **Hsu, S.-K.** and **Su, C.C.** (2023) Changes in Kuroshio Current dynamics and East Asian monsoon variability during the last 26 kyr. *Palaeogeogr. Palaeoclimatol. Palaeoecol.*, **632**, 111836.

Feuillet, N., **Beauducel, F.** and **Tapponnier, P.** (2011) Tectonic context of moderate to large historical earthquakes in the Lesser Antilles and mechanical coupling with volcanoes. *J. Geophys. Res. Solid Earth*, **116**, 89–153.

Francois, R., **Frank, M.**, **Rutgers van der Loeff, M.M.** and **Bacon, M.P.** (2004) ^{230}Th normalization: An essential tool for interpreting sedimentary fluxes during the late Quaternary. *Paleoceanography*, **19**, PA 1018.

Fujita, R., **Goto, K.**, **Iryu, Y.** and **Abe, T.** (2020) Millennial paleotsunami history at Minna Island, southern Ryukyu Islands, Japan. *Prog Earth Planet Sci*, **7**, 1–15.

Fujiwara, K., **Kawamura, R.** and **Kawano, T.** (2020a) Remote thermodynamic impact of the Kuroshio current on a developing tropical cyclone over the Western North Pacific in Boreal fall. *J. Geophys. Res. Atmos.*, **125**, e2019JD031356.

Fujiwara, O., **Goto, K.**, **Ando, R.** and **Garrett, E.** (2020b) Paleotsunami research along the Nankai Trough and Ryukyu Trench subduction zones–current achievements and future challenges. *Earth Sci. Rev.*, **210**, 103333.

Garzanti, E., **Nayak, K.**, **Padoan, M.**, **Vezzoli, G.**, **Resentini, A.**, **Castelltort, S.**, **Lin, A.**, **Babonneau, N.**, **Ratzov, G.**, **Hsu, S.-K.** and **Huang, K.F.** (2023) Fast-eroding Taiwan and transfer of orogenic sediment to forearc basins and trenches in the Philippine and South China seas. *Earth-Science Reviews*, **244**, 104523.

Goldfinger, C. (2011) Submarine paleoseismology based on turbidite records. *Ann. Rev. Mar. Sci.*, **3**, 35–66.

Goldfinger, C., **Nelson, C.H.**, **Johnson, J.E.** and **Party, S.S.** (2003) Holocene earthquake records from the Cascadia subduction zone and northern San Andreas fault based on precise dating of offshore turbidites. *Annu. Rev. Earth Planet. Sci.*, **31**, 555–577.

Goldfinger, C., **Nelson, C.H.**, **Morey, A.E.**, **Johnson, J.E.**, **Patton, J.R.**, **Karabanov, E.B.**, **Gutierrez-Pastor, J.**, **Eriksson, A.T.**, **Gracia, E.**, **Dunhill, G.**, **Enkin, R.J.**, **Dallimore, A.** and **Vallier, T.** (2012) *Turbidite Event History—Methods and Implications for Holocene Paleoseismicity of the Cascadia Subduction Zone (No. 1661-F)*. US Geological Survey, Reston, VA.

Goto, K., **Kawana, T.** and **Imamura, F.** (2010a) Historical and geological evidences of boulders deposited by tsunamis, southern Ryukyu Islands, Japan. *Earth Sci. Rev.*, **102**, 77–99.

Goto, K., **Miyagi, K.**, **Kawamata, H.** and **Imamura, F.** (2010b) Discrimination of boulders deposited by tsunamis and storm waves at Ishigaki Island, Japan. *Mar. Geol.*, **269**, 34–45.

Goto, K., **Miyagi, K.** and **Imamura, F.** (2013) Localized tsunamigenic earthquakes inferred from preferential distribution of coastal boulders on Ryukyu Islands, Japan. *Geology*, **41**, 1139–1142.

Guinasso, N.L. and **Schink, D.R.** (1975) Quantitative estimates of Biological Mixing Rates in Abyssal Sediments. *J. Geophys. Res.*, **80**, 3032–3043.

He, S., **Cheng, X.**, **Fei, J.**, **Wei, Z.**, **Huang, X.** and **Liu, L.** (2022) Thermal response to tropical cyclones over the Kuroshio. *Earth Space Sci.*, **9**, e2021EA002001.

Heaton, T.J., **Köhler, P.**, **Butzin, M.**, **Bard, E.**, **Reimer, R.W.**, **Austin, W.E.**, **Bronk Ramsay, C.**, **Grootes, P.M.**, **Hughen, K.**, **A.**, **Kromer, B.**, **Reimer, P.J.**, **Adkins, J.**, **Burke, A.**, **Cook, M.S.**, **Olsen, J.** and **Skinner, L.C.** (2020) Marine20—the marine radiocarbon age calibration curve (0–55,000 cal BP). *Radiocarbon*, **62**, 779–820.

Henderson, G.M. and **Anderson, R.F.** (2003) The U-series toolbox for paleoceanography. *Reviews in Mineralogy and Geochemistry*, **52**(1), 493–531.

Heywood, L.J., **DeBari, S.M.**, **Gill, J.B.**, **Straub, S.M.**, **Schindlbeck-Belo, J.C.**, **Escobar-Burciaga, R.D.** and **Woodhead, J.** (2020) Across-arc diversity in rhyolites from an intra-oceanic arc: Evidence from IODP Site U1437, Izu-Bonin rear arc, and surrounding area. *Geochem. Geophys. Geosyst.*, **21**, e2019GC008353.

Hickey-Vargas, R. (1998) Origin of the Indian Ocean-type isotopic signature in basalts from Philippine Sea plate spreading centers: An assessment of local versus large-scale processes. *J. Geophys. Res. Solid Earth*, **103**, 20963–20979.

Hsiung, K.H., **Kanamatsu, T.**, **Ikehara, K.**, **Shiraishi, K.**, **Horng, C.S.** and **Usami, K.** (2017) Morpho-sedimentary features and sediment dispersal systems of the southwest end of the Ryukyu Trench: a source-to-sink approach. *Geo-Mar. Lett.*, **37**, 561–577.

Hsu, S.-K. and **Sibuet, J.-C.** (2005) Earthquake off Japan could generate strong tsunami. *Eos*, **86**, 169–170.

Hsu, S.K., **Yeh, Y.C.**, **Sibuet, J.C.**, **Doo, W.B.** and **Tsai, C.H.** (2013) A mega-splay fault system and tsunami hazard in the southern Ryukyu subduction zone. *Earth Planet. Sci. Lett.*, **362**, 99–107.

Hu, D., **Wu, L.**, **Cai, W.**, **Gupta, A.S.**, **Ganachaud, A.**, **Qiu, B.**, **Gordon, A.L.**, **Lin, X.**, **Chen, Z.**, **Hu, S.**, **Wang, G.**, **Wang, Q.**, **Sprintall, J.**, **Qu, T.**, **Kashino, Y.**, **Wang, F.** and **Kessler, W.S.** (2015) Pacific western boundary currents and their roles in climate. *Nature*, **522**, 299–308.

Huh, C.-A., **Su, C.-C.**, **Liang, W.-T.** and **Ling, C.-Y.** (2004) Linkages between turbidites in the southern Okinawa Trough and submarine earthquakes. *Geophys. Res. Lett.*, **31**, L12304.

Huh, C.-A., **Su, C.-C.**, **Wang, C.-H.**, **Lee, S.-Y.** and **Lin, I.-T.** (2006) Sedimentation in the Southern Okinawa Trough - Rates, turbidites and a sediment budget. *Mar. Geol.*, **231**, 129–139.

Ikehara, K., **Kanamatsu, T.**, **Nagahashi, Y.**, **Strasser, M.**, **Fink, H.**, **Usami, K.**, **Irino, T.** and **Wefer, G.** (2016) Documenting large earthquakes similar to the 2011 Tohoku-oki earthquake from sediments deposited in the Japan Trench over the past 1500 years. *Earth Planet. Sci. Lett.*, **445**, 48–56.

Ikehara, K., **Usami, K.**, **Kanamatsu, T.**, **Arai, K.**, **Yamaguchi, A.** and **Fukuchi, R.** (2018) Spatial variability in sediment lithology and sedimentary processes along the Japan Trench: use of deep-sea turbidite records to reconstruct past large earthquakes. In: *Tsunamis: Geology, Hazards and Risks* (Eds Scourse, E.M., Chapman, N.A., Tappin, D.R. and Wallis, S.R.), *Geological Society, London, Special Publications*, **456**, 75–89.

Ikehara, K., **Kanamatsu, T.** and **Usami, K.** (2022) Possible Tsunami-Induced Sediment Transport From Coral Reef to Deep Sea Through Submarine Canyons on the Southern Ryukyu Forearc, Japan. *Front. Earth Sci.*, **10**, 753583.

Kanamatsu, T., **Ikehara, K.** and **Misawa, A.** (2020) Seafloor morphology and sediment magnetic fabric in a putative 1771 Meiwa tsunami source region in the southern Ryukyu Islands, SW Japan. In: *Characterization of Modern and Historical Seismic–Tsunamic Events, and their Global–Societal Impacts* (Eds Dilek, Y., Ogawa, Y. and Okubo, Y.), *Geological Society, London, Special Publications*, **501**, 156–189.

Kanamatsu, T., **Ikehara, K.** and **Hsiung, K.H.** (2022) Stratigraphy of deep-sea marine sediment using paleomagnetic secular variation: Refined dating of turbidite relating to giant earthquake in Japan Trench. *Mar. Geol.*, **443**, 106669.

Kao, H. (1998) Can great earthquakes occur in the southernmost Ryukyu arc-Taiwan region. *Terr. Atmos. Ocean. Sci*, **9**, 487–508.

Kawamura, K., **Oguri, K.**, **Inoue, M.**, **Hsiung, K.H.**, **Kudaka, T.** and **Takai, K.** (2023) Ongoing persistent slope failures at the toe of a giant submarine slide in the Ryukyu Trench that generated the AD 1771 Meiwa Tsunami. In: *Progress in Landslide Research and Technology* (Ed. Alcántara-Ayala, I.). Springer, Cham.

Kawana, T. and **Nakata, T.** (1994) Timing of late Holocene tsunamis originated around the southern Ryukyu Islands, Japan, deduced from coralline tsunami deposits. *J. Geogr. (Chigaku Zasshi)*, **103**, 352–376.

Kemnitz, S., **Hammond, D.M.**, **Henderson, D.E.**, **Le Roy, E.**, **Charette, M.**, **Moore, W.**, **Anderson, R.F.**, **Fleisher, M.Q.**, **Leal, A.**, **Black, E.**, **Hayes, C.T.**, **Adkins, J.**, **Berelson, W.** and **Bian, X.** (2023) Actinium and radium fluxes from the seabed in the northeast Pacific Basin. *Mar. Chem.*, **250**, 104180.

Kim, R.A., **Lee, K.E.** and **Bae, S.W.** (2015) Sea surface temperature proxies (alkenones, foraminiferal Mg/Ca, and planktonic foraminiferal assemblage) and their implications in the Okinawa Trough. *Prog Earth Planet Sci*, **2**, 12059.

Kimura, J.-I., **Nagahashi, Y.**, **Satoguchi, Y.** and **Chang, Q.** (2015) Origins of felsic magmas in Japanese subduction zone: geochemical characterizations of tephras from caldera forming eruptions <5 Ma. *Geochem. Geophys. Geosyst.*, **16**, 2147–2174.

Kuritani, T. (2023) Geochemical constraints on the evolution of the magmatic system leading to catastrophic eruptions at Aira Caldera, Japan. *Lithos*, **450**, 107208.

Lai, Y.M., **Song, S.R.**, **Lo, C.H.**, **Lin, T.H.**, **Chu, M.F.** and **Chung, S.L.** (2017) Age, geochemical and isotopic variations in volcanic rocks from the Coastal Range of Taiwan: Implications for magma generation in the Northern Luzon Arc. *Lithos*, **272**, 92–115.

Lallemand, S. (1996) ACT cruise, RV L'Atalante. https://doi.org/10.17600/96010040.

Lallemand, S. and **Liu, C.-S.** (1998) Geodynamic implications of present-day kinematics in the southern Ryukyus. *J. Geol. Soc. China*, **41**, 551–564.

Lallemand, S., **Liu, C.-S.**, **Dominguez, S.**, **Schnürle, P.**, **Malavieille, J.** and **the ACT scientific crew** (1999) Trench-parallel stretching and folding of forearc basins and lateral migration of the accretionary wedge in the southern Ryukyus: a case of strain partition caused by oblique convergence. *Tectonics*, **18**, 231–247.

Lallemand, S., **Font, Y.**, **Bijwaard, H.** and **Kao, H.** (2001) New insights on 3-D plates interaction near Taiwan from tomography and tectonic implications. *Tectonophysics*, **335**, 229–253.

Lallemand, S., **Theunissen, T.**, **Schnürle, P.**, **Lee, C.-S.**, **Liu, C.-S.** and **Font, Y.** (2013) Indentation of the Philippine Sea Plate by the Eurasia Plate in Taiwan: details from recent marine seismological experiments. *Tectonophysics*, **594**, 60–79.

Lambeck, K., **Rouby, H.**, **Purcell, A.**, **Sun, Y.** and **Sambridge, M.** (2014) Sea level and global ice volumes from the last Glacial Maximum to the Holocene. *Proc. Natl. Acad. Sci.*, **111**, 15296–15303.

Le Maitre, R.W., **Streckeisen, A.**, **Zanettin, B.**, **Le Bas, M.J.**, **Bonin, B.**, **Bateman, P.**, **Bellieni, G.**, **Dudek, A.**, **Efremova, S.**, **Keller, J.**, **Lameyre, J.**, **Sabine, P.A.**, **Schmid, R.**, **Sorensen, H.** and **Woolley, A.R.** (2002) *Igneous rocks. A Classification and Glossary of Terms: Recommendations of the International Union of Geological Sciences Subcommission on the Systematics of Igneous Rocks*. Cambridge University Press, Cambridge.

Lehu, R., **Lallemand, S.**, **Hsu, S.K.**, **Babonneau, N.**, **Ratzov, G.**, **Lin, A.T.** and **Dezileau, L.** (2015) Deep-sea sedimentation offshore eastern Taiwan: facies and processes characterization. *Mar. Geol.*, **369**, 1–18.

Lehu, R., **Lallemand, S.**, **Ratzov, G.**, **Babonneau, N.**, **Hsu, S.K.**, **Lin, A.T.** and **Dezileau, L.** (2016) An attempt to reconstruct

2700 years of seismicity using deep-sea turbidites offshore eastern Taiwan. *Tectonophysics*, **692**, 309–324.

Li, X., **Zeng, Z.**, **Chen, S.**, **Ma, Y.**, **Yang, H.**, **Zhang, Y.** and **Chen, Z.** (2018) Geochemical and Sr-Nd-Pb isotopic compositions of volcanic rocks from the Iheya Ridge, the middle Okinawa Trough: Implications for petrogenesis and a mantle source. *Acta Oceanologica Sinica*, **37**, 73–88.

Lisiecki, L.E. and **Raymo, M.E.** (2005) A Pliocene-Pleistocene stack of 57 globally distributed benthic δ18O records. *Paleoceanography*, **20**, 356.

Liu, X. and **Wei, J.** (2015) Understanding surface and subsurface temperature changes induced by tropical cyclones in the Kuroshio. *Ocean Dyn.*, **65**, 1017–1027.

Liu, J., **Chen, Z.**, **Chen, M.**, **Yan, W.**, **Xiang, R.** and **Tang, X.** (2010) Magnetic susceptibility variations and provenance of surface sediments in the South China Sea. *Sediment. Geol.*, **230**, 77–85.

Machida, H. (2002) Volcanoes and tephras in the Japan area. *Glob. Environ. Res.*, **6**, 19–28.

Matsu'ura, T. and **Ueno, T.** (2022) Late Quaternary tephrostratigraphy and pollen stratigraphy of Uwa Formation, Shikoku Island, SW Japan: Reconsidering the MIS 11 super-interglacial horizon. *Quat Geochronol.*, **73**, 101383.

Matsu'ura, T., **Ikehara, M.** and **Ueno, T.** (2021) Late Quaternary tephrostratigraphy and cryptotephrostratigraphy of core MD012422: improving marine tephrostratigraphy of the NW Pacific. *Quat. Sci. Rev.*, **257**, 106808.

McCarthy, A., **Yogodzinski, G.**, **Tepley, F.J., III**, **Bizimis, M.**, **Arculus, R.** and **Ishizuka, O.** (2019) Isotopic characteristics of Neogene-Quaternary tephra from IODP Site U1438: A record of explosive volcanic activity in the Kyushu-Ryukyu arc. *Geochem. Geophys. Geosyst.*, **20**, 2318–2333.

McDonough, W.F. and **Sun, S.S.** (1995) The composition of the Earth. *Chem. Geol.*, **120**, 223–253.

McHugh, C.M., **Kanamatsu, T.**, **Seeber, L.**, **Bopp, R.**, **Cormier, M.H.** and **Usami, K.** (2016) Remobilization of surficial slope sediment triggered by the A.D. 2011M w 9 Tohoku-Oki earthquake and tsunami along the Japan Trench. *Geology*, **44**, 391–394.

McHugh, C.M., **Seeber, L.**, **Rasbury, T.**, **Strasser, M.**, **Kioka, A.**, **Kanamatsu, T.**, **Ikehara, K.** and **Usami, K.** (2020) Isotopic and sedimentary signature of megathrust ruptures along the Japan subduction margin. *Mar. Geol.*, **428**, 106283.

McLean, D., **Albert, P.G.**, **Nakagawa, T.**, **Suzuki, T.**, **Staff, R.A.**, **Yamada, K.**, **Kikaba, I.**, **Yamasaki, A.**, **Haraguchi, T.**, **Kitagawa, J.**, **SG14 Project Members** and **Smith, V.C.** (2018) Integrating the Holocene tephrostratigraphy for East Asia using a high-resolution cryptotephra study from Lake Suigetsu (SG14 core), central Japan. *Quat. Sci. Rev.*, **183**, 36–58.

McLean, D., **Albert, P.G.**, **Suzuki, T.**, **Nakagawa, T.**, **Kimura, J.I.**, **Chang, Q.** and **Smith, V.C.** (2020) Constraints on the timing of explosive volcanism at Aso and Aira calderas (Japan) between 50 and 30 ka: New insights from the Lake Suigetsu sedimentary record (SG14 core). *Geochem. Geophys. Geosyst.*, **21**, e2019GC008874.

Miyazawa, K., **Goto, K.** and **Imamura, F.** (2012) Re-evaluation of the 1771 Meiwa tsunami source model, southern Ryukyu Islands, Japan. In: *Submarine Mass Movements and their Consequences: 5th International Symposium*, pp. 497–506. Springer, Dordrecht.

Mukasa, S.B., **Flower, M.F.** and **Miklius, A.** (1994) The Nd-, Sr-and Pb-isotopic character of lavas from Taal, Laguna de Bay and Arayat volcanoes, southwestern Luzon, Philippines: implications for arc magma petrogenesis. *Tectonophysics*, **235**, 205–221.

Mulder, T. and **Cochonat, P.** (1996) Classification of offshore mass movements. *J. Sediment. Res.*, **66**, 43–57.

Nakamura, M. (2009) Fault model of the 1771 Yaeyama earthquake along the Ryukyu Trench estimated from the devastating tsunami. *Geophys. Res. Lett.*, **36**, 458.

Nayak, K., **Lin, A.T.-S.**, **Huang, K.-F.**, **Liu, Z.**, **Babonneau, N.**, **Ratzov, G.**, **Pillutla, R.K.**, **Das, P.** and **Hsu, S.-K.** (2021) Clay-mineral distribution in recent deep-sea sediments around Taiwan: implications for sediment dispersal processes. *Tectonophysics*, **814**, 228974.

Okamura, Y., **Nishizawa, A.**, **Fujii, Y.** and **Yanagisawa, H.** (2018) Accretionary prism collapse: a new hypothesis on the source of the 1771 giant tsunami in the Ryukyu Arc, SW Japan. *Sci. Rep.*, **8**, 13620.

Omoto, K. (2012) Distribution of coral boulders beached by huge tsunamis and calibrated radiocarbon ages of fossil *Porites* sp. of Maibahabama, SE of Miyako Island, Okinawa Prefecture. *J. Geogr.*, **121**, 1043–1051.

Pan, J., **Feng, X.**, **Lai, W.**, **Devlin, A.T.** and **Lin, H.** (2018) Barrier effects of the Kuroshio current on the East Asian Northerly Monsoon: a sensitivity analysis. *Sci. Rep.*, **8**, 18044.

Patton, J.R., **Goldfinger, C.**, **Morey, A.E.**, **Ikehara, K.**, **Romsos, C.**, **Stoner, J.**, **Djadjaduhardja, Y.**, **Udrekh, A.**, **Ardhyastuti, S.**, **Zulkarnaen, E.** and **Vizcaino, A.** (2015) A 6600 year earthquake history in the region of the 2004 Sumatra-Andaman subduction zone earthquake. *Geosphere*, **11**, 2067–2129.

Pizer, C.O., **Howarth, J.D.**, **Clark, K.J.**, **Orpin, A.R.**, **Tickle, S.E.**, **Strachan, L.J.**, **Barnes, P.**, **Camp, S.**, **Mckeown, M.** and **Twort, E.** (2024) Integrated onshore–offshore paleoseismic records show multiple slip styles on the plate interface, central Hikurangi subduction margin, Aotearoa New Zealand. *Quat. Sci. Rev.*, **344**, 108942.

Polonia, A., **Panieri, G.**, **Gasperini, L.**, **Gasparotto, G.**, **Bellucci, L.G.** and **Torelli, L.** (2012) Turbidite paleoseismology in the Calabrian Arc Subduction Complex (Ionian Sea). *G3*, **14**(1), 112–140.

Pouderoux, H., **Proust, J.N.** and **Lamarche, G.** (2014) Submarine paleoseismology of the northern Hikurangi subduction margin of New Zealand as deduced from Turbidite record since 16 ka. *Quatern. Sci. Rev.*, **84**, 116–131.

Richter, T.O., **Van der Gaast, S.**, **Koster, B.**, **Vaars, A.**, **Gieles, R.**, **de Stigter, H.C.**, **de Haas, H.** and **van Weering, T.C.** (2006) The Avaatech XRF Core Scanner: technical description and applications to NE Atlantic sediments. In: *New Techniques in Sediment Core Analysis* (Ed. Rothwell, R.G.), *Geological Society, London, Special Publications*, **267**, 39–50.

Rothwell, R.G. and **Croudace, I.W.** (2015) Twenty years of XRF core scanning marine sediments: what do geochemical proxies tell us? In: *Micro-XRF Studies of Sediment Cores: Applications of a Non-Destructive Tool for the Environmental Sciences* (Eds Croudace, I.W. and Rothwell, R.G.), pp. 25–102. Springer Netherlands, Dordrecht.

San Pedro, L., **Babonneau, N.**, **Gutscher, M.A.** and **Cattaneo, A.** (2017) Origin and chronology of the Augias deposit in the Ionian Sea (Central Mediterranean Sea), based on new regional sedimentological data. *Mar. Geol.*, **384**, 199–213.

Sasaki, Y.N., **Minobe, S.**, **Asai, T.** and **Inatsu, M.** (2012) Influence of the Kuroshio in the East China Sea on the early Summer (Baiu) rain. *J. Climate*, **25**, 6627–6645.

Seibert, C., **Feuillet, N.**, **Ratzov, G.**, **Beck, C.**, **Morena, P.**, **Johannes, L.**, **Ducassou, E.**, **Cattaneo, A.**, **Goldfinger, C.**, **Moreno, E.**, **Biebern, A.**, **Bénatre, G.**, **Caron, B.**, **Caron, M.**, **Casse, M.**, **Cavailhes, T.**, **Del Manzo, G.**, **Deschamps, C.E.**, **Desiage, P.A.**, **Doboc, Q.**, **Fauquembergue, K.**, **Ferrant, A.**, **Guyard, H.**, **Jacques, E.**, **Laurencin, M.**, **Leclerc, F.**, **Patton, J.**, **Saurel, J.M.**, **St-Onge, G.** and **Woerther, P.** (2024) Sedimentary Records in the Lesser Antilles Fore-Arc Basins Provide Evidence of Large Late Quaternary Megathrust Earthquakes. *Geochem. Geophys. Geosyst.*, **25**, e2023GC011152.

Shinjo, R. and **Kato, Y.** (2000) Geochemical constraints on the origin of bimodal magmatism at the Okinawa Trough, an incipient back-arc basin. *Lithos*, **54**, 117–137.

Shinjo, R., **Chung, S.L.**, **Kato, Y.** and **Kimura, M.** (1999) Geochemical and Sr-Nd isotopic characteristics of volcanic rocks from the Okinawa Trough and Ryukyu Arc: Implications for the evolution of a young, intracontinental back arc basin. *J. Geophys. Res.*, **104**, 10591–10608.

Shinjo, R., **Woodhead, J.D.** and **Hergt, J.M.** (2000) Geochemical variation within the northern Ryukyu Arc: magma source compositions and geodynamic implications. *Contrib. Mineral. Petrol.*, **140**, 263–282.

Smith, V.C., **Staff, R.A.**, **Blockley, S.P.**, **Bronk Ramsey, C.**, **Nakagawa, T.**, **Mark, D.F.**, **Takemura, K.**, **Danhara, T.** and **Suigetsu 2006 Project members** (2013) Identification and correlation of visible tephras in the Lake Suigetsu SG06 sedimentary archive, Japan: chronostratigraphic markers for synchronising of east Asian/west Pacific palaeoclimatic records across the last 150 ka. *Quat. Sci. Rev.*, **67**, 121–137.

Spratt, R.M. and **Lisiecki, L.E.** (2016) A Late Pleistocene sea level stack. *Climate Past*, **12**, 1079–1092.

Stow, D.A., **Howell, D.G.** and **Nelson, C.H.** (1985) Sedimentary, tectonic, and sea-level controls. In: *Submarine Fans and Related Turbidite Systems*, pp. 15–22. Springer, New York, NY.

Strasser, M., **Ikehara, K.**, **Pizer, C.**, **Itaki, T.**, **Satoguchi, Y.**, **Kioka, A.**, **McHugh, C.**, **Proust, J.-N.**, **Sawyer, D.** and **IODP Expedition 386** (2024) Japan Trench event stratigraphy: First results from IODP giant piston coring in a deep-sea trench to advance subduction zone paleoseismology. *Mar. Geol.*, **477**, 107387.

Stuiver, M., **Reimer, P.J.** and **Braziunas, T.F.** (1998) High-precision radiocarbon age calibration for terrestrial and marine samples. *Radiocarbon*, **40**, 1127–1151.

Suzuki, A., **Yokoyama, Y.**, **Kan, H.**, **Minoshima, K.**, **Matsuzaki, H.**, **Hamanaka, N.** and **Kawahata, H.** (2008) Identification of 1771 Meiwa Tsunami deposits using a combi- nation of radiocarbon dating and oxygen isotope microprofiling of emerged massive Porites boulders. *Quat. Geochronol.*, **3**, 226–234.

Theunissen, T., **Font, Y.**, **Lallemand, S.** and **Liang, W.T.** (2010) The largest instrumentally recorded earthquake in Taiwan: revised location and magnitude, and tectonic significance of the 1920 event. *Geophys. J. Int.*, **183**, 1119–1133.

Tsuji, Y. (1993) Tide influenced high energy environments and rhodolith-associated carbonate deposition on the outer shelf and slope off the Miyako Islands, southern Ryukyu Island Arc, Japan. *Mar. Geol.*, **113**, 255–271.

Tsuji, T., **Ikeda, M.**, **Furusawa, A.**, **Nakamura, C.**, **Ichikawa, K.**, **Yanagida, M.**, **Nishizaka, N.**, **Ohnishi, K.** and **Ohno, Y.** (2018) High resolution record of Quaternary explosive volcanism recorded in fluvio-lacustrine sediments of the Uwa basin, southwest Japan. *Quat. Int.*, **471**, 278–297.

Ujiie, H. and **Ujiie, Y.** (1999) Late Quaternary course changes of the Kuroshio current in the Ryukyu Arc region, northwestern Pacific Ocean. *Mar. Micropaleontol.*, **37**, 23–40.

Ujiie, H., **Nakamura, T.**, **Miyamoto, Y.**, **Park, J.-O.**, **Hyun, S.** and **Oyakawa, T.** (1997) Holocene turbidite cores from the southern Ryukyu Trench slope: suggestions of periodic earthquakes. *J. Geol. Soc. Japan*, **103**, 590–603.

Ujiie, Y., **Ujiie, H.**, **Taira, A.**, **Nakamura, T.** and **Oguri, K.** (2003) Spatial and temporal variability of surface water in the Kuroshio source region, Pacific Ocean, over the past 21,000 years: evidence from planktonic foraminifera. *Mar. Micropaleontol.*, **49**, 335–364.

Ujiie, Y., **Asahi, H.**, **Sagawa, T.** and **Bassinot, F.** (2016) Evolution of the North Pacific Subtropical Gyre during the past 190 kyr through the interaction of the Kuroshio Current with the surface and intermediate waters. *Paleoceanography*, **31**, 1498–1513.

Usami, K., **Ikehara, K.**, **Kanamatsu, T.** and **McHugh, C.M.** (2018) Supercycle in great earthquake recurrence along the Japan Trench over the last 4000 years. *Geosci. Letters*, **5**, 1–12.

Van Daele, M., **Meyer, I.**, **Moernaut, J.**, **De Decker, S.**, **Verschuren, D.** and **De Batist, M.** (2017) A revised classification and terminology for stacked and amalgamated turbidites in environments dominated by (hemi) pelagic sedimentation. *Sediment. Geol.*, **357**, 72–82.

Wu, C.-R., **Chang, Y.-L.**, **Oey, L.-Y.**, **Chang, C.-W.J.** and **Hsin, Y.-C.** (2008) Air-sea interaction between tropical cyclone Nari and Kuroshio. *Geophys. Res. Lett.*, **35**, 3942.

Wu, L., **Wilson, D.J.**, **Wang, R.**, **Yin, X.**, **Chen, Z.**, **Xiao, W.** and **Huang, M.** (2020) Evaluating Zr/Rb Ratio from XRF Scanning as an Indicator of Grain-Size Variations of Glaciomarine Sediments in the Southern Ocean. *Geochem. Geophys. Geosyst.*, **21**, 458.

Xu, X. and **Ujiie, H.** (1994) Bathyal benthic foraminiferal changes during the past 210,000 years: Evidence from piston cores taken from seas south of Ishigaki Island, Southern Ryukyu Island. In: *Transactions and Proceedings of the Paleontological Society of Japan*, Vol. **1994**, pp. 497–520. Palaeontological Society of Japan, Tokyo.

Yamamoto, M. (2008) Trace of earthquake and tsunami in Ishigaki Island, Yaeyama Archipelago. *Archaeol. J. Japan*, **577**, 9–14 (in Japanese).

Yang, H.-S., **Nozaki, Y.**, **Sakai, H.**, **Nagaya, Y.** and **Nakamura, K.** (1986) Natural and man-made radionuclide distributions in Northwest Pacific deep-sea sediments: rates of sedimentation, bioturbation and ^{226}Ra migration. *Geochem. J.*, **20**, 29–40.

Yoneda, M., **Uno, H.**, **Shibata, Y.**, **Suzuki, R.**, **Kumamoto, Y.**, **Yoshida, K.**, **Sasaki, T.**, **Suzuki, A.** and **Kawahata, H.** (2007) Radiocarbon marine reservoir ages in the western Pacific estimated by pre-bomb molluscan shells. *Nucl. Instrum. Methods Phys. Res., Sect. B*, **259**, 432–437.

Manuscript received 27 July 2024; revision accepted 13 August 2025

Supporting Information

Additional information may be found in the online version of this article:

Data S1. Analytical techniques and data for U-and Th-series analyses of boxcore sediments.

Data S2. Characterisation and geochemical data (major, trace elements and isotopes) of tephra deposits.

Data S3. Oxygen Isotope measurements along MD18-3530 and MD18-3531.

Data S4. Detailed sedimentary successions of the cores MD18-3528, MD18-3529, MD18-3530 and MD18-3531.